Identification of nuclear pore proteins at plasmodesmata: potential role in intercellular transport?

T. Moritz Schladt[1,*, §], Manuel Miras[1,3,*], Jona Obinna Ejike[1,2,*], Mathieu Pottier[1,4,*], Lin Xi[5], Andrea Restrepo-Escobar[1,], Masayoshi Nakamura[6,7], Niklas Pütz[1], Sebastian Hänsch[2,8], Chen Gao[1], Julia Engelhorn[1,2], Marcel Dickmanns[1,9], Gwendolyn V. Davis[1], Ahan Dalal[1,2], Sven Gombos[5], Ronja Lange[1], Rüdiger Simon[2,9], Waltraud X. Schulze[5] & Wolf B. Frommer[1,2,6,§]

[1] Heinrich Heine University Düsseldorf, Faculty of Mathematics and Natural Sciences, Institute for Molecular Physiology, 40225 Düsseldorf, Germany
[2] Cluster of Excellence on Plant Sciences, Heinrich Heine University Düsseldorf, 40225 Düsseldorf, Germany
[3] New address: Department of Stress Biology and Plant Pathology, CEBAS-CSIC, E-30100 Murcia, Spain
[4] New address: Université de Lorraine, INRAE, IAM, F-54000 Nancy, France
[5] Department of Plant Systems Biology, University of Hohenheim, 70593 Stuttgart, Germany
[6] Institute for Transformative Biomolecules (WPI-ITbM), Nagoya University, 464-860 Nagoya, Japan
[7] New address: Department of Biochemistry and Molecular Biology, Saitama University, 330-8570 Saitama, Japan
[8] Center for Advanced Imaging; Heinrich Heine University Düsseldorf, 40225 Düsseldorf, Germany
[9] Department of Molecular Structural Biology, Max Planck Institute of Biochemistry, Martinsried, Germany
[10] Heinrich Heine University Düsseldorf, Faculty of Mathematics and Natural Sciences, Institute of Developmental Genetics, 40225 Düsseldorf, Germany

* Equal contribution
§ For correspondence: schladti@hhu.de, frommew@hhu.de

Abstract

Plasmodesmata (PD) mediate intercellular exchange of small molecules, RNAs and proteins between plant cells with an apparent exclusion limit for passive non-specific transport, and transport of specific cargo mediated by mediators. PD and nuclear pore complexes (NPC) are nanometer sized micropores with strikingly similar properties. Cargo translocation through NPC is mediated by phase separating FG-nucleoporins (FG-NUP). Here, bioinformatics, proteomics and fluorescence imaging identified FG-NUPs at PD. Transient expression of GFP fusions at low and intermediate expression levels supported dual localization of 12 NUPs to NPC and PD. Structured illumination microscopy detected the transmembrane anchor NUP CPR5 close to orifices of PD. *cpr5* mutants showed reduced intercellular short-root (SHR) transport. However, transport defects cannot be excluded due to indirect effects in the mutants. Identification of FG-NUPs at PD is consistent with the recruitment of NUPs to form a PD pore gating complex consistent with phase separation domains as diffusion barriers at PD. Further analyses will be required to determine whether NUPs are *bona fide* PD components, or accumulate at PD in certain conditions, or may serve intermediate NPC storage.

Introduction

Nutrient exchange and communication between cells are essential for multicellular organisms. Besides membrane transporters and cell surface receptors, metazoa, fungi and plants independently evolved cell-cell bridges. The green lineage developed unique structures, called plasmodesmata (PD), composed of modified cell wall domains that form plasma membrane-lined channels and that contain an ER-derived desmotubule providing continuity between the cytoplasm of neighboring cells (symplasm). Since PD are embedded into the cell wall and contain diverse membrane and soluble proteins, PD pose a major challenge for biochemical and cell biological analyses. Several studies obtained PD proteomes by enriching membrane proteins in cell wall fractions (Bayer et al., 2006; Brault et al., 2019; Fernandez-Calvino et al., 2011; Gombos et al., 2023). Genetic approaches failed so far to identify proteins that could fully explain the transport mechanism, possibly due to redundancy or lethality of mutants. Intercellular transport studies are also challenging since intact at minimum, a functional two cell system is required. Current models for PD translocation implicate a simple filter mechanism generated by spoke-like structures connecting the peripheral plasma membrane with the desmotubule, however the complex transport properties as well as inconsistencies such as the finding that sleeveless PD lacking an obvious path may put these models in question.

Key features of PD transport include the ability to translocate highly diverse cargo (from ions to macromolecules), an apparent size exclusion limit (which, depending of the type of PD, can reach 70 kDa, in funnel PD up to 120 kDa), and the ability to translocate specific cargo (Paultre et al., 2016; Ross-Elliott et al., 2017). Translocation through PD and the nuclear pore complex (NPC) share common features, namely both NPC and PD transport a similar spectrum of cargo species (ions, metabolites, proteins, and ribonucleoprotein complexes)(Ejike et al., 2025; Lee et al., 2000). For both NPC and PD, the ability for pore dilation has been described (Kragler et al., 1998; Zimmerli et al., 2021). Both NPC and PD constitute selective barriers, allowing '*passive passage of molecules'* with an apparent size exclusion limit (term used in animal literature; named '*non-targeted movement*' for PD) and '*facilitated translocation of specific macromolecules'* ('*targeted movement*' for PD)(Crawford and Zambryski, 2001; Frey et al., 2018). Notably, the surface properties of cargo proteins play an important role for translocation, allowing even tetrameric GFP variants with compatible surface properties to pass (Frey et al., 2018). The core of the permeability barrier of the NPC appears to be a separated phase / condensate formed by disordered phenylalanine–glycine (FG) repeat-containing proteins, the FG-nucleoporins (Frey et al., 2018; Hoogenboom et al., 2021; Ng et al., 2021; Yu et al., 2023). These smart sieves mediate passage of smaller molecules without interaction with the FG repeats, while larger molecules or specific cargo can pass with the help of nuclear transport receptors that specifically interact with the FG repeats (Kehlenbach et al., 2023). As a shared structure among eukaryotes, the ultrastructure, function and transport mechanism of the NPC is well understood (Ejike et al., 2025; Mosalaganti et al., 2022). The human NPC, with about 1000 polypeptides, has an approx. diameter of 120 nm, a pore size of ~43 nm and a height of 80 nm generated by membrane-anchors, three stacked rings (a sandwich of two outer and one inner ring), cytoplasmic filaments, and a nucleocytoplasmic basket (Lin and Hoelz, 2019). The human genome encodes twelve FG-nucleoporins (NUPs): NUP42, NUP50, NUP54, NUP58 (aka NUP45), NUP62, NUP98, NUP153, NUP214, POM121, POM121B, POM121C, and NUP358(Terry and Wente, 2009), while plant genomes encode ten FG-NUPs: NUP42 (aka CG1), NUP50a & NUP50b, NUP54, NUP58, NUP62, NUP98a & NUP98b, NUP136 and NUP214 (Chopra et al., 2019; Makarov et al., 2021). The majority of the FG-NUPs were conserved, with only three FG-NUPs lost in the green lineage (NUP153, POM121, NUP358).

FG-NUPs and other NUPs in PD fractions of *Physcomitrium patens* and localization to PD

Based on the striking similarities in transport properties, we hypothesized that PD transport may use permeability barriers similar as the NPC, that is, phase-separation generated by FG-repeat proteins. We thus explored whether the green lineage evolved a distinct set of FG-repeat containing proteins. A bioinformatic search for FG repeat-containing proteins in the genome of the moss *P. patens* revealed that 12 out of the 15 top-ranked FG-containing proteins were NUPs; the other three proteins were not considered candidates for a transport function (table S1; file S1; file S2 for Arabidopsis FG-containing proteins). An alternative hypothesis was that the PD permeability barrier is generated by NUPs derived by tandem gene duplications followed by differentiation into NPC and PD functions. However,

phylogenetic analyses of Arabidopsis *NUPs* showed that the majority of NUPs are encoded by single genes (see also table S2 for overview of Arabidopsis *NUPs*)(Makarov et al., 2021; Zhang et al., 2020). Interestingly, however, the PD proteome from *P. patens* contained FG-NUP50a and two other NUPs, SEC13 and NUA (Gombos et al., 2023). Since PD cannot be purified to homogeneity, we cannot exclude that these NUPs represent contaminations. Previous work had indicated that *bona-fide* moss PD proteins can be targeted to PD when expressed in tobacco leaves (Gombos et al., 2023). To test whether FG-NUPs localize exclusively to the NPC or can also be targeted to PD, the subcellular localization of fluorescent protein (FP) fusions of three *P. patens* FG-NUPs (NUP58, NUP62 and NUP98) was analyzed by confocal microscopy after β-estradiol-controlled transient expression in *Nicotiana benthamiana*. A substantial number of fluorescent puncta derived from C-terminal mVenus fusions of the three FG-NUPs overlaid with fluorescent puncta of aniline blue marking callose at PD (Figure 1A; Figure1-figure supplement 1). PD localization did not appear to be due to an FG-NUPs-specific mis-localization, since the inner ring linker NUP35, which connects the transmembrane interaction hub with the ALADIN-NDC1 core to NUP155, also localized to PD (Figure 1A). Of note, the fluorescent puncta derived from mVenus fusions in the periphery did not exclusively localize to aniline blue labeled PD pit fields. Fluorescent mVenus and aniline blue derived puncta were also separately detected in locations without overlay. It is known that aniline blue does not detect all pit fields (Huang et al., 2022). Notably, transient expression in *N. benthamiana*, even though controlled by use of an estrogen-inducible system, can lead to overexpression; thus, the observed localization could either represent a physiologically relevant site for accumulation when under conditions of excess, or be due to accumulation in the vicinity of PD orifices.

FG-NUPs and other NUPs in PD fractions of Arabidopsis

To explore whether FG-NUPs may also be present in PD fractions from a vascular plant, we utilized established PD enrichment and data analysis pipelines to generate a PD proteome from Arabidopsis shoots (Gombos et al., 2023). This shoot PD proteome had an overlap of 80% with published PD proteomes and included ~43% of known high-confidence PD proteins, e.g., the well-established plasmodesmata-located proteins (PDLP) and multiple C2 domains and transmembrane region proteins (MCTP) PD markers (table S3, Figure 1-figure supplement 2 and 3, file S3)(Brault et al., 2019; Thomas et al., 2008). The Arabidopsis PD-enriched fraction included seven Arabidopsis FG-NUPs (Figure 1B). Moreover, inner and outer ring and basket NUPs were found in the high-confidence PD protein list (Figure 1B). In total, 20 proteins from different NPC domains were identified. 15 proteins were enriched in PD fractions compared to cell wall and total Arabidopsis protein fractions (Figure 1B, C, Figure 1-figure supplement 2 and 3). Several of the identified nuclear pore components passed the threshold for consideration as high-confidence PD proteins, in particular proteins of the inner and outer rings, core and basket. High-confidence PD scoring was based on enrichment in biochemical PD fractions as well as on an iterative weighting process which factors in features of known PD-localized proteins (Gombos et al. 2023). Separation of PD scores of "likely PD proteins" and likely contaminants (here: plastidic and mitochondrial proteins)(Fernandez-Calvino et al., 2011; Gombos et al., 2023) was significant, allowing to define confidence scores. NUP proteins were also previously identified in PD proteome preparation (Figure 1-figure supplement 2E). In particular NUPs such as FG-NUPs NUP62, NUP214, NUP50a, as well as CPR5, GP210, NUP35, NUP93a, NUP155, NUP205, NUP43, HOS1 (aka HOS1/ELYS), SEC13, and NUP82 were found in proteomics data of cell wall/PD protein fractions from other studies (table S4)(Bayer et al., 2006; Fernandez-Calvino et al., 2011; Gombos et al., 2023; Kirk et al., 2022; Kraner et al., 2017). While the detection of a large number of NUPs including FG-NUPs in the PD fractions, even with enrichment, may support a possible role in PD functions, we can not exclude that they represent contaminants.

Localization of Arabidopsis FG-NUPs and other NUPs to PD

To explore whether Arabidopsis FG-NUP-mVenus fusions can be detected at PD, candidates were expressed from an β-estradiol-inducible promoter in *N. benthamiana* leaves, which can be used to limit overexpression. Fluorescence derived from FP-fusions of the FG-NUP58, FG-NUP62 and FG-NUP98b overlaid with aniline blue fluorescent puncta (with a significantly higher PD index relative to that for the non-specific cell wall dye propidium iodide, Figure 2, Figure 2-figure supplement 1, table S2), indicating that Arabidopsis FG-NUPs can be targeted to PD. Notably, 12 out of a total of the 16 NUPs tested here localized to puncta in the cell periphery that overlaid with aniline blue fluorescence at pit fields (Figure 2, Figure 3A, B; Figure 2-figure supplement 1)(Zavaliev and Epel, 2015). Overall, 12 NUPs showed

significant enrichment at PD compared to the cell wall marker (Figure 2B, Figure 3B, table S2), including two outer ring NUPs (NUP43, HOS1/ELYS) and two transmembrane NUPs (GP210, CPR5) (Figure 1C, 3B). Ten NUP fusions for various inner and outer ring and membrane anchor NUPs were also detected in nuclei (Figure 2-figure supplement 1, list of 16 tested NUPs: table S2). Fluorescent puncta of aniline blue and FP-fusions of PD protein typically do not provide a perfect colocalization since aniline blue staining does not mark all PD and typically, the overlay is partial since FP-fusions are not detected at all PD even for high confidence PD proteins (Pendle and Benitez-Alfonso, 2015). As an independent line of evidence we observed overlay of the PD marker PDLP5-mScarlet3 and an mCitrine fusion of the putative NUP107-160 complex recruitment factor HOS1/ELYS at PD (Figure 3G). To test for potential artifacts, caused possibly by mistargeting due to overexpression, the concentration of the inducer β-estradiol and the induction time were reduced. In plants expressing NUP43-mCitrine or CPR5-FP fusions, the fluorescence intensity was reduced (Figure 3D,E), without negatively affecting dual NUP localization at NPC and PD (example for NUP43-mCitrine in Figure 3C). The fluorescence ratio between periphery and nucleus did not differ significantly after expression induction by 2 µM compared to 20 µM β-estradiol (Figure 3F). The resolution of confocal imaging is insufficient to conclude that the NUPs localize inside PD or accumulate in the vicinity. We also cannot exclude that expression of the NUP fusions leads to mis-targeting to PD. Different from data obtained for NUP98a (Gallemí et al., 2016), a C-terminal mVenus fusion to the auto-cleavable NUP98b was fluorescent and localized to PD (Figure 2, Figure 2-figure supplement 1), indicating that either under the condition used in our experiments, the main fraction of NUP98b was unprocessed, or that the C-terminal peptide reassociated with the N-terminal domain of NUP98b, as previously described for the two splice forms of the human NUP98 (Hodel et al., 2002). Out of 16 NUPs tested, four NUPs did not localize at PD, as indicated by non-significant PD indices over the cell wall marker (p-values > 0.08, table S2). Out of 35 currently known Arabidopsis NUPs, 19 NUPs were not yet tested here (table S2).

Single copy insertions of GFP-fusions in stable transformants reduce the potential for artifacts caused by overexpression. Analysis of nine independent stably transformed homozygous single insertion Arabidopsis lines expressing a full-length genomic FG-NUP62-GFP fusion under the control of the native NUP62 promoter showed dual localization of the protein to the nuclei and PD. However, PD-specific localization was only detected in mature cotyledons older than 10 days (Figure 2C, D). Notably, the peripheral localization of NUP62-GFP was not restricted solely to PDs, as punctate fluorescence was detected at the cell surface, outside of PD regions (Figure 2E). Importantly, these punctate fluorescent signals at the cell periphery, encompassing both PD-associated and non-PD-associated localization, were absent in roots and in young leaves approximately 4 days old (Figure 2D). Although the single insertion Arabidopsis lines tested here should have FG-NUP62-GFP levels closer to native conditions than the heterologous overexpression of FG-NUP62-mVenus in *N. benthamiana*, it cannot be excluded that the levels in tested lines are still higher than the native levels, or that the fluorescence protein fused to the NUP affects localization.

Components of the inner ring, NUP93a and NUP155, and the basket, NUP82, were also detected at PD when heterologously overexpressed in *N. benthamiana*, although with lower confidence compared to, e.g., CPR5. Analysis of published data from other groups, who had localized NUPs to nuclei also showed peripheral puncta, which had not been analyzed further (table S5). As of now, we cannot exclude that the localization in the periphery is an overexpression artifact due to accumulation in the ER at the orifices of PD since the complexes are too large for translocation (Giordano et al., 2013). Alternatively, the puncta in the periphery could be the consequence of an accumulation, when biotic or abiotic conditions lead to elevated production of NUPs that cannot replace existing NUPs, similar to annulate lamellae (AL). In such conditions, the peripheral accumulation might serve as cellular storage of excessive NUPs. Interestingly, in mammalian cells, depletion of NUP98 led to FG-NUP accumulation sites in the periphery at ER junctions. Such sites of accumulation may serve as NUP storage depots rather than sites of degradation (Pletan et al., 2025).

Topology of CPR5, a potential membrane anchor at both NPC and PD

Since the phase separation domain in the nuclear pore is produced by ten FG-NUPs and PD appear to contain multiple FG-NUPs, it may be necessary to mutate multiple *FG-NUP* genes before it is possible to observe intercellular transport defects (Xiao et al., 2020). It is also conceivable that *knock-out* mutants

in multiple *FG-NUPs* may be lethal. We thus rather focused on the green lineage-specific membrane anchor CPR5, a nuclear pore component with a high PD index of 1.48 (Figure 3, table S2). Four potential membrane proteins that anchor the human NPC in the nuclear membrane had been identified: GP210, POM121, NDC1 and TMEM33. Arabidopsis encodes genes for three anchors GP210, NDC1 and PNET1 (homolog of human TMEM209; table S6), while CPR5 had been proposed to serve as an anchor in the equatorial plane of the NPC (Apelt et al., 2016; Gu et al., 2016). Since CPR5 was among the top 5 candidates based on the PD index, one may hypothesize that it may serve as an anchor for an NPC-like structure at PD (Figure 3A, B, Figure 2-figure supplement 1). CPR5, a polytopic membrane protein, is predicted to form a globular helix bundle domain at its N-terminus, flanked by disordered regions and connected to a 105 amino acid α-helix (Figure 4-figure supplement 1). The central helix contains a hydrophobic region, which, together with four shorter hydrophobic helices, forms an approximately 35 Å long transmembrane domain, consistent with the expected thickness of ER membranes. The C-terminus possibly extends into the ER lumen. While it has been considered that CPR5 may play specialized roles, e.g., in defense reactions, it is also conceivable that the phenotypes are secondary defects (Arra et al., 2024; Gu et al., 2016; Ma et al., 2023; Peng et al., 2022), caused by the missing anchoring activity (Apelt et al., 2016; Gu et al., 2016). CPR5 is encoded by a single gene in Arabidopsis and two in rice (Figure 4-figure supplement 2, table S6, table S7)(Arra et al., 2024). In PD, CPR5 could either be embedded into the plasma membrane near or at PD, with the C-terminus facing the apoplasm, or into the ER/desmotubule membrane, with its C-terminus facing the desmotubule lumen (or ER lumen in the vicinity of PD) and the long N-terminal domain pointing into the intermembrane space of PD/cytosol, analogous to the CPR5 topology in the ER-derived nuclear membrane at the NPC. A split-GFP system for topology studies of membrane proteins was used to determine whether the C-terminus of CPR5 faces the luminal side of the ER (Xie et al., 2017). When an N-terminal GFP11 fusion to CPR5 was co-expressed with a free cytosolic GFP1-10, fluorescence was reconstituted, consistent with the N-terminus being located in the cytosol or the cytosolic sleeve of PD (Figure 4A; Figure 4-figure supplement 3). A control using a GFP1-10 domain targeted to and retained in the ER lumen (GFP1-10-HDEL) did not show detectable fluorescence reconstitution (Figure 4B). The complementary fusion of GFP11 to the C-terminus of CPR5 led to reconstitution of fluorescence when co-expressed with an ER lumen targeted GFP1-10-HDEL, but not when co-expressed with a cytosolic GFP1-10 (Figure 4A, B; Figure 4-figure supplement 3). The topological data are consistent with a model in which the C-terminal five-helix-bundle of CPR5 traverses the ER/desmotubule membrane with the C-terminus inside the lumen of the ER/desmotubule, while the extended central α-helix, the predicted unstructured domains, and the smaller helical bundle of CPR5 are located in the intermembrane space between the ER/desmotubule and the plasma membrane (Figure 4-figure supplement 1).

Localization of CPR5 at the orifices of PD

A hypothetical NPC-like structure could serve as a micropore in the PD channel, or be present close to the PD entrance. To determine CPR5 localization in the PD at higher resolution, we performed structured illumination microscopy (SIM) with a CPR5-mCitrine fusion. CPR5 was found to localize adjacent to aniline blue labeled callose deposition at PD. Therefore, CPR5 may localize to or near the neck region of PD, but not in the central cavity of the PD, where a PDLP5-mScarlet3 was localized (Figure 4C, D; Figure 4-figure supplement 4)(Fitzgibbon et al., 2010). These findings are consistent with a model in which NUPs are present at or close to the PD orifices. We did not observe puncta at both paired neck regions in all cases (Figure 4-figure supplement 4B, top), possibly due to mosaic-like expression in *N. benthamiana*, in which only one of the adjacent cells expressed the fusion protein (model: Figure 4D). CPR5-mCitrine localization was absent at some PD (Figure 4-figure supplement 4B, *bottom*): in 10 images from 3 independent repeats, CPR5-mCitrine and PDLP5-mScarlet3 localized to 76 ± 6% and 81 ± 10% of the aniline blue labeled pit fields, respectively, while CPR5-mCitrine localized to 79 ± 9% of the PDLP5-mScarlet3 puncta (Figure 4-figure supplement 4D). Note that CPR5-mCitrine also localized in the periphery outside PD (Figure 4-figure supplement 4D).

Intercellular transport defects in *cpr5* mutants

If indeed NUPs form phase-separated barriers at PD to control cell-to-cell transport, and given the defects of *cpr5* mutants in nuclear transport, one may expect that interference with CPR5 function might impair *facilitated and non-facilitated cell-to-cell translocation of specific macromolecules*. Particle

bombardment of Arabidopsis leaves was performed to transiently express a tandem-GFP fusion (2xmEGFP; 54 kDa) in two independent *cpr5* loss-of-function mutants (EMS mutant *cpr5-1* (G420D) and T-DNA insertion mutant *cpr5-T3* ; Figure 5-figure supplement 1C, D)(Bowling et al., 1997; Crawford and Zambryski, 2000; Faulkner et al., 2013; Gu et al., 2016; Otero et al., 2016; Sakulkoo et al., 2018; Wang et al., 2017). Cell-to-cell movement of 2xmEGFP was significantly reduced in the *cpr5* mutants relative to wild type (WT) (Figure 5A, B; Figure 5-figure supplement 1A, B). Originally named for its *constitutive pathogen response* phenotype, loss of CPR5 activity can trigger constitutive defense responses that could cause callose deposition and closure of PD (Kohler et al., 2002), however, callose levels were not significantly different (Figure 5C).

The transcription factor SHORT-ROOT (SHR), produced in cells of the stele, migrates into the endodermis by *facilitated cell-to-cell translocation,* followed by nuclear import (Nakajima et al., 2001). Intercellular transport of SHR is crucial for tissue patterning (Koizumi et al., 2012; Nakajima et al., 2001; Winter et al., 2024). To explore whether SHR-GFP (86.6 kDa) movement was impacted in a *cpr5* loss-of-function mutant, we compared the endodermis-to-stele ratio (E:S ratio) of GFP fluorescence intensity in roots of homozygous *shr* mutants expressing pSHR:SHR–GFP in WT, as well as in the *cpr5-1* mutant background. The E:S ratio was significantly reduced in *cpr5-1* compared to WT, consistent with a defect in facilitated SHR transport across PD (Figure 5D, E). Fluorescence recovery after photobleaching (FRAP) of nuclei in the root endodermis of homozygous *shr*/pSHR:SHR lines in *cpr5-1* was significantly lower compared to WT, further supporting that targeted transport across PD is reduced in *cpr5-1* (Figure 5F,G, Figure 5-figure supplement 1F). Notably, no significant difference in SHR–GFP fluorescence intensity was observed in the steles of WT when compared to *cpr5-1* lines (Figure 5-figure supplement 1E). The *cpr5* mutants showed no detectable defect in small molecule transport indicative of WT-like PD density and preservation of the capability to mediate small molecule transport as shown by 'Drop-ANd-See' *trans*-leaf diffusion assays (DANS, carboxyfluorescein: 376 Da; control CaMV*35S:PDLP5*; Figure 5H, I)(Lee et al., 2011). In summary, the intercellular transport assay results indicate that a callose-independent transport mechanism for macromolecules is defective in *cpr5* mutants. While consistent with a possible contribution of NUPs to intercellular transport, we cannot exclude that the reduced transport is due to secondary effects in the *cpr5* mutants, which show rather severe phenotypic defects (Figure 5-figure supplement 1C, D).

Discussion

Based on the observations that (i) a substantial number of NUPs were identified in PD-enriched cell wall fractions, (ii) 12/35 known plant NUPs, including multiple FG-NUPs, localized to PD, and (iii) intercellular tandem-GFP and SHR transport was reduced in *cpr5* mutants could indicate that components of the NPC may generate a complex that can sustain a similar phase separation domain at PD as found in the NPC, and that phase separation generated by FG-NUPs may play a role in intercellular translocation (Kehlenbach et al., 2023). Previous studies had shown that cargo size cannot be the only criterion for cell-to-cell transport efficiency through PD (Alazem et al., 2025; Campbell et al., 2025; Howell et al., 2024; Kragler et al., 1998; Lee et al., 2003). The evidence for PD localization of NUPs obtained here is intriguing, as it may provide new potential explanations for the underlying mechanism of transport of certain mobile molecules (e.g. RNA-protein complexes) that are larger than the expected size exclusion limit (Tee and Faulkner, 2024). In this context the discovery of a new function of the nuclear transport receptor importin α4 as a PD-associated protein in mediating systemic infection of a plant virus in rice may further support the hypothesis of NPC-like transport functions (Lu et al., 2025).

Nuclear transport experiments using surface modified GFPs and analysis of the properties of nuclear transport receptors indicate that the phase separated domain generated by FG-NUPs in the permeation pathway of the NPC facilitates the transit of cargo that carry arginines, cysteines, histidines, and hydrophobic amino acids at their surface (Ejike et al., 2025; Frey et al., 2018). It will be very informative to test whether similar cargo surface properties are important for the transport through PD. Transport assays combined with pharmacological approaches using compounds such as hexanediol, which disrupt phase-separated domains, and systematic analyses of transport using surface-modified FPs of the same size (Frey et al., 2018; Ng et al., 2023) might help identifying phase separated domains at PD.

In summary we found three independent lines of evidence for the presence of NUPs at or near PD in the context of this work, based on subcellular localization, proteomics, and transport. However, all three independent lines could potentially be the result of artifacts. In particular, we found NUP localization at PD in overexpression conditions and, interestingly, also in stable transgenic Arabidopsis lines with presumably lower protein levels. However, NUP localization in the Arabidopsis lines at PD has only been observed in mature cotyledons and so far not in other tissues such as younger leaves or root. We can not exclude that in the NUP62-GFP lines, PD localization of NUPs is caused by elevated protein levels. Alternatively, it might be possible that localization of NUPs at PD occurs at (natively) elevated protein levels and/or depends on factors such as growth condition, pathogen infection and hormones, which were shown to influence mRNA levels of NUPs (Ascencio-Ibanez et al., 2008; Chen et al., 2012; Narsai et al., 2011; Okuma et al., 2014; Song et al., 2009). Interestingly, dynamic changes in subcellular localization of NUPs in response to environmental stimuli were reported previously, e.g., HOS1-GFP re-localizes from the periphery to the nucleoplasm after cold treatment (Lee et al., 2001). Perhaps the PD localization of NUPs is dynamic, occurring only under certain environmental conditions. To validate the subcellular localization, additional evidence is needed from stable transgenic lines with NUP fusions expressed under the control of the native promoter and terminator, complementing the NUP mutant background, and grown in different environmental conditions. Specific antisera raised against plant NUPs that are suitable for immunolocalization may help to clarify the subcellular localization of NUPs under native conditions. New insights may also be generated by cryo-electron tomography, for which recently suitable protocols have been established (Pöge et al., 2025). An alternative hypothesis that also implicates LLPS for the PD permeability barrier is based on the finding that the linker between the N-terminal C2A and C2B domains (C2A-B linker domain) of multiple C2 domains and transmembrane region proteins (MCTP) found in PD is predicted to be disordered and show strong intrinsic propensity for liquid-liquid phase separation (Dickmanns et al., 2025). Cryo-electron microcopy of plasmodesmata identified assemblies that decorate the desmotubule, which are likely formed by MCTPs, and which could then form an extended permeability barrier in the PD pore (Dickmanns et al., 2025).

There is evidence for NUPs to constitute a permeability barrier between cytoplasm and cilia (ciliary transition zone) in animal cells (Blasius et al., 2019; del Viso et al., 2016; Gu et al., 2016; Takao et al., 2017). However, the exact composition of the proposed ciliary pore complex and its anchoring at the ciliary base remains a matter of debate, as cryo-ET structures of the ciliary base/ transition zone are not yet available (Johnson and Malicki, 2019). Similarly, the assembly of NUPs at PD must differ from that at the NPC because, as described above, desmotubules extend through the central channel of PD and the cytoplasmic sleeve width at PD is smaller than the pore width at the NPC (Ejike et al., 2025; Mosalaganti et al., 2022; Nicolas et al., 2017). The localization of the same NUPs at PD as well as nuclear pores is unexpected, given that one would rather expect gene duplication and diversification to enable independent regulation. Note that not all known NUPs were tested here, and some of those tested did not localize to the PD. The structure, function and regulation of the predicted PD pore complex (PDPC) may differ from that of the NPC.

NUPs seem to also play functional roles outside the NPC in animal cells: FG-NUPs were found in several cyto- and nucleoplasmic membrane-less organelles, such as P-bodies, P-granules, stress granules, and viral-associated organelles. In animals, annulate lamellae, preassembled NPCs in ER stacks, are characteristic for rapidly dividing cells during germ cell development, early embryogenesis and cancerogenic growth and might serve as storage place for NUPs (Kessel, 1992; Penzo and Palancade, 2023). AL have also been found in plant cells (Scheer and Franke, 1972). High NUP levels could result in accumulation within AL. Missing an organellar marker for AL, we cannot exclude that fluorescent puncta derived from NUP-FP fusions in our subcellular localization experiments indicate NUP localization to AL. However, the arrangement of fluorescent puncta did not follow a stacking pattern, which we would expect because of the stacked ER sheets in AL.

PD are challenging research subjects due to the embedding into the cell wall, and the presence of multiple membranes. Based on the similarities between transport properties of PD and NPC, one may hypothesize that they both use similar transport mechanisms. Further characterization will be required to explore mechanisms for delivery of a diverse set of GFP-fused NUPs to PD, and to evaluate their localization and

trafficking, e.g. by immunolocalization. Alternatively, accumulation could serve as transient storage of NPC complexes, or are a consequence of overaccumulation at the constriction of ER at PD entrances.

Materials and Methods

Plant materials and growth conditions

Physcomitrium patens (*P. patens*) ecotype Grandsen cultures were obtained from the *International Moss Stock Center (IMSC)* (Freiburg). *P. patens* was cultured in liquid cultures of modified BCD medium as described (Gombos et al., 2023). The BCD medium consisted of the following solutions which were mixed prior to use: Solution B (0.1 mM $MgSO_4 \cdot 7H_2O$), Solution C (1.84 mM KH_2PO_4), Solution DK (1 M KNO_3), Solution DF (4.5 mM $FeSO_4 \cdot 7H_2O$), Trace Element Solution (TES) (614 mg H_3BO_3, 55 mg $CuSO_4 \cdot 5H_20$, 28 mg KBr, 110 mg $Al_2(SO_4)3 \cdot K_2SO_4 \cdot 24H_20$, 389 mg $MnCl_2 \cdot 4H_20$, 55 mg $ZnSO_4 \cdot 7H_20$, 28mg LiCl, 10 mM $CoCl_2 \cdot 6H_20$, 28 mg KI and 28 mg $SnCl_2 \cdot 2H_20$ in 1 L H_20), 500 mM diammonium tartrate and 1 M $CaCl_2$. For liquid cultures, 1% (m/v) glucose was added. For propagation of liquid cultures, moss was homogenized and then transferred to 100 ml medium in a 250 ml. Cultures were harvested after two weeks of growth at 21°C under long day conditions (16 h light/8 h dark) at ~90 µmol m^{-2} sec^{-1}, 60% humidity.

Arabidopsis *cpr5-1* (G420D) mutant and *cpr5-T3* (SALK_074631) T-DNA insertion mutant were kindly provided by Dr. Gu (University of California Berkeley) and Professor Chun-Hai Dong (Qingdao Agricultural University), respectively (Bowling et al., 1994; Wang et al., 2017). Arabidopsis Col-0 *shr*/pSHR:SHR–GFP line was described before (Cui et al., 2007) and kindly gifted by Ikram Blilou, KAUST. The pSHR:SHR–GFP/*cpr5-1* in the *shr* mutant background was generated by crossing, and identified in the F2 segregating generation by sequencing of CPR5. For quantification of the SHR-GFP endodermis-to-stele ratio, F5 seedlings of the Arabidopsis lines pSHR:SHR–GFP *cpr5-1* were grown on a glass plate coated with ½ salt strength Murashige and Skoog (MS) media agar [half-strength Murashige and Skoog basal salt mixture (Duchefa Biochemie, Haarlem, The Netherlands), 0.1 % (w/v) 2-(N-morpholino)-ethanesulfonic acid, 1.5% agar, pH 5.6] (Dyachok et al., 2010) for 6 days in short day conditions (10 h light, 14 h darkness), at 21°C with a light intensity to 130 µmol m^{-2} s^{-1}. For microparticle bombardment assays and callose quantification, Arabidopsis Col-0, *cpr5-1,* and *cpr5-T3* plants were grown on ½ MS plates in the same conditions as described above for 4 weeks. Nine independent stably transformed homozygous Arabidopsis wildtype lines with single insertions for NUP62-GFP were used for fluorescence imaging (T3 segregants; 3:1 segregation) and grown on ½ MS media supplemented with 1% (w/v) sucrose and 1% (w/v) agar in a growth chamber (16 h light/8 h darkness, 23 °C, 50 µmol m^{-2} $s^{-1}$of white light, 60% humidity). For DANS assay, Arabidopsis WT and T-DNA insertion lines were grown in soil with one plant per pot at 21°C under long day conditions (16 h light/8 h dark) for 3 weeks. For analyses of the Arabidopsis shoot proteome, plants were grown in soil at 21°C under long day conditions (16 h light/8 h dark) at ~90 µmol m^{-2} sec^{-1}, 60% humidity. Respective tissues were harvested after three or five weeks. *Nicotiana benthamiana* (*N. benthamiana*) plants were grown individually in a pot under controlled conditions (16 h light/8 h darkness, 26 °C, ~90 µmol m^{-2} s^{-1}, 60% humidity).

DNA constructs

For transient expression in *N. benthamiana*, the selected NUP open reading frames (ORFs) were cloned into the binary pAB134-mVenus plasmid (Bleckmann et al., 2010). To generate the ORFs, total RNA was extracted from Arabidopsis leaves using the RNeasy plant mini kit (Qiagen, Hilden, Germany), and DNase I treatment was performed following the manufacturer's instructions. cDNA was then synthesized using the Maxima H Minus First Strand cDNA synthesis kit (Thermo Fisher Scientific Inc., Waltham, Massachusetts, USA). The ORFs were amplified, incorporating the Gateway attB sites, and purified PCR products were cloned into pDONR221 using a BP clonase reaction (Thermo Fisher Scientific Inc., Waltham, Massachusetts, USA). *E. coli* Stellar cells (Takara Bio) were transformed with the resulting entry vectors. Plasmids with the correct sequence were isolated and then recombined by LR reaction into the binary plant expression vector pAB134-mVenus as C-terminal mVenus fusions under the control of a β-estradiol-inducible promoter (Bleckmann et al., 2010). For localization of PpNUP35.1, Pp3c6_16260V3 was amplified and cloned into the binary pAB134-mVenus plasmid. For SIM experiments, XVE:CPR5-mCitrine and XVE:PDLP5-mScarlet3 were generated using GreenGate (Lampropoulos et al., 2013). CPR5 and PDLP5 genomic sequences were amplified with primers including

*Bsa*I restriction sites and ligated to pGGC000 previously digested with *Bsa*I. Resulting vectors were used to generate expression constructs using the GreenGate modules: XVE promoter (module A), CPR5 or PDLP5 (module C), C-mCitrine or mScarlet3 (module D), HSP18.2-Terminator (module E), and the pOLE1:OLE1-RFP seed coat selection marker (Shimada et al., 2010) (module F) were ligated to the linearized binary vector pGGZ003.

Monomeric enhanced GFP (mEGFP) and 2xmEGFP sequences were amplified by PCR from plasmids pENTR-R4R3-mEGFP-C (Addgene #113749) and pGGC025 (Addgene #48830), respectively, using Gateway specific primers adding the attB1 and attB2 sites and cloned into pDONR221 by BP reaction (Thermo Fisher Scientific Inc., Waltham, Massachusetts, USA). The resulting constructs, pDONR221-mEGFP and pDONR221-2xmEGFP were used for LR reaction into the destination vector pGWB502 (Addgene #74844). The p35S:3xmCherry construct was generated using GreenGate by ligating the modules Ca MV 35S promoter (Addgene #48815) (module A), 3xmCherry (Addgene #48831) (module C), HSP18.2-Terminator (module E), and the pOLE1:OLE1-RFP seed coat selection marker (module F) into the linearized binary vector pGGZ003. Topology localization of CPR5 was carried out using the split-GFP system with the vectors kindly provided by Prof. Thordal-Christensen (University of Copenhagen) (Xie et al., 2017). pDONR-CPR5 plasmid was recombined into pDest-GW-GFP11 and pDest-GFP11-GW to generate either N- and C- fusions to the GFP 11th β-sheet using LR Gateway reactions (Thermo Fisher Scientific Inc., Waltham, Massachusetts, USA). The GFP1-10 fragment was co-expressed with either cytosolic localization (GFP1-10) or with ER-luminal localization (GFP1-10-HDEL). Plasmids pEG100-35S:nYFP-CPR5, pEG100-35S:cYFP-CPR5 and pEG100-35S:NUP93a-cYFP used for homo- and hetero-oligomerization were kindly gifted by Prof. Xinnian Dong (Duke University. North Carolina, USA) (Gu et al., 2016). The nYFP fragment contains residues 1-172, and cYFP consists of residues 173-238. A translational fusion NUP62-GFP construct was generated from a genomic clone of *NUP62* (At2g45000), including a 1135-bp region 5'-upstream from the initiation ATG and a 407-bp region 3'-downstream from the stop codon. mEGFP was fused to the NUP62 separated by a GGGGSGGGGSGGGGS-linker (Shimozono and Miyawaki, 2008), just before the stop codon using NEBuilder® HiFi DNA Assembly (NEB). The fluorescent protein-fusion construct was digested by *Not*I and integrated into the pBIN40 binary vector (Miyashima et al., 2011). The final binary vectors were introduced into *Agrobacterium tumefaciens* strain GV3101:pMP90 and used to carry out the transformation of Arabidopsis.

We confirmed the nucleotide sequences of all constructs using standard DNA manipulation and sequencing techniques. Primers used in this study are listed in table S8.

Transient expression in *N. benthamiana* leaves

The *Agrobacterium tumefaciens* strain GV3101 (pMP90, pSOUP), containing the desired construct, was cultured overnight, then diluted to 1/10 and grown until the culture reached an OD_{600} of 0.6-0.8. Cultures were pelleted by centrifuge at 4000 rpm for 10 minutes. Bacteria were subsequently re-suspended in an Infiltration Buffer comprising 0.01 M 2-(N-morpholino) ethanesulfonic acid (MES) at pH 5.6, 0.01 M $MgCl_2$, and 150 µM acetosyringone at a final OD_{600} of 0.3. The *Agrobacterium* strain containing the intended construct was then combined with an *Agrobacterium* strain containing the P19 silencing suppressor (OD_{600} 0.1) (Qu and Morris, 2002). The resulting mixture was introduced into the leaves of 4-week-old *N. benthamiana* plants through syringe infiltration. Two days after infiltration, gene expression was induced by spraying infiltrated leaves with β-estradiol solution (20 µM β-estradiol, 0.1% v/v Tween-20). Induction time was dependent on protein maturation times and ranged from 6 to 24 h. To test localization of XVE:NUP43-mCitrine or XVE:CPR5-FP fusions at lower expression levels induction was performed with 2 µM β-estradiol and induction times did not exceed 10 h (2 µM β-estradiol, 0.1% v/v Tween-20).

For split-GFP assays, agrobacterial cultures were suspended in the Infiltration Buffer at a final OD_{600} of 0.3. *Agrobacterium* strains containing constructs split-GFP were co-infiltrated with the P19 silencing suppressor (OD_{600} 0.1) into *N. benthamiana* leaves. For split-GFP assays either GFP11-CPR5 or CPR5-GFP11 and GFP1-10 or GFP1-10-HDEL were co-infiltrated. Samples were imaged 2 days post infiltration.

Microscopy

Subcellular localization of FP fusions by confocal microcopy

Confocal microscopy was performed on a Zeiss LSM 900 (Carl Zeiss, Oberkochen, Germany) equipped with Airyscan GaAsP-PMT detectors and diode lasers using a 40x/1.20 water immersion objective (C-Apochromat 40x/1.20 W Korr FCS). mCitrine or mVenus were excited with a 488 nm laser and emission was collected in a 520-579 nm window. GFP was excited at 488 nm and collected in a 500-550 nm window. mScarlet3 was excited at 561 nm and collected from 579-617 nm (Gadella et al., 2023). To visualize pit fields, *N. benthamiana* leaves expressing a protein of interest were infiltrated with 0.1% (w/v) aniline blue (Sigma Aldrich) solution and then imaged (excitation at 405 nm and 3-5% laser power, emission detected in a 440-480 nm window). Free mScarlet3 was expressed and excited to visualize cytoplasmic localization. Propidium iodide, a cell impermeant dye, stains the apoplasm when short incubation times are used. Thus, for visualization of the cell wall, shortly before the experiment, PI was pipetted on the object slide on the leaf disc (excitation 561 nm, 6% laser power, emission 574-617 nm). Pit fields in cotyledons of 8-day old transgenic NUP62-GFP Arabidopsis seedlings were stained by immersing leaves in 0.5% aniline blue in Sørensen's phosphate buffer [0.5% aniline blue (w/v) in 200 mM Sørensen's phosphate buffer prepared with Na_2HPO_4 and NaH_2PO_4 pH 8, Sigma-Aldrich, Saint Louis, Missouri, USA)]. For confocal imaging of NUP62-GFP Arabidopsis lines, an Eclipse Ti2 inverted microscope (Nikon) equipped with spinning disk confocal unit CSU-10 (Yokogawa) and a sCMOS camera PRIME 95B (Photometrics, Tuscon, AZ, USA) was used. GFP was excited with a 488-nm laser, and emission was collected with a 525/50-nm filter (Semrock, Rochester, New York). Images were taken with a 100x oil-immersion lens (CFI Plan Apo Lambda 1.45 NA, Nikon).

Structured Illumination Microscopy

For structured illumination microscopy (SIM), only pit fields that were not deeply embedded in the plant tissue and most proximal to the cover glass close to the objective, were observed. To do so, a *N. benthamiana* leaf disk (2-mm diameter) was immersed in water and pressed between an object slide and a high-precision coverslip (1.5H, 18 x 18 mm; A. Hartenstein) using a magnet. The sample chamber was sealed with a flexible mounting adhesive (Fixo gum; Marabu). Z-stacks with a scaling of 149-nm steps were obtained using an Elyra PS1 (Zeiss Microscopy GmbH, Oberkochen, Germany) equipped with a C-Apochromat 63x/1.2 water-immersion M27 objective. Frame size was 512 x 512 pixels. PDLP5-mScarlet3, CPR5-mCitrine, and aniline blue were excited with 561 nm, 488 nm, and 405 nm laser wavelengths, respectively. Detection filters were set for the different channels: aniline blue: bandpass (BP) 420–480/LP 750; CPR5-mCitrine: BP 495–570/LP 750; PDLP5-mScarlet3: BP 570-650/LP 655. In initial control experiments with the Elyra PS1, we observed more puncta in the green channel after excitation at 488 nm, after having used the 405 nm laser to excite aniline blue. These additional puncta in the green channel precisely overlayed with the puncta observed in the aniline blue channel. The identification of fluorescent puncta in this channel in response to excitation of aniline blue might be the result of photoconversion to longer wavelengths. To exclude possible artifacts due to photoconversion of the aniline blue, which could lead to emission in the channels used for detection of mCitrine, sequential excitation was performed at 561, 488 and 405 nm. The grating periods (grid size) for structured illumination were set to 34, 34, and 28 µm, respectively, for the three different laser wavelengths. The number of grid rotations was set to 3 rotations. Camera exposure time ranged from 49-128 ms. The setup was operated using Zeiss ZEN 2.3 SP1 software. An internal deconvolution program for SIM z-stacks was used in 3D mode with maximum isotropy, zero sectioning, and the baseline shift active for all three excitation channels. The noise filter was initially run in automatic mode, but was set to a unit below the automatic setting for the actual processing.

Callose quantification in Arabidopsis seedlings

CPR5 is involved in the activation of pattern triggered immunity (PTI) and in the repression of effector-triggered immunity (ETI) (Ma et al., 2023; Wang et al., 2014). The *cpr5-1* mutant had previously been reported to show constitutive resistance to two virulent pathogens (Bowling et al., 1997). An important plant defense mechanism against pathogens is induction of callose deposition at PD. Elevated callose deposition in the *cpr5*-1 mutant after wounding has been reported (Kohler et al., 2002). To test whether callose deposition was increased relative to WT under the growth and experimental conditions used here, PD callose levels in WT and *cpr5-1* Arabidopsis seedlings were quantified. Leaf 5 of young seedlings (8-

12 leaf stage) was stained to minimize variability. Leaves were detached with a forceps, immersed in 1% aniline blue diluted in water [1% aniline blue (w/v); Sigma-Aldrich, Saint Louis, Missouri, USA] and infiltrated by applying a vacuum in a 20 ml syringe. Aniline blue fluorescence was observed on a Zeiss LSM 900 (Zeiss Microscopy GmbH, Oberkochen, Germany) C-Apochromat 40x/1.20 W Korr FCS and GaAsP-Pmt1 detector with excitation at 405 nm, 5% laser power and gain at 632 V. Emission was detected from 400-500 nm. Imaging parameters were consistent across all experiments. Per experiment, 3-4 leaves were assayed per genotype, 4 images were acquired per leaf. Four independent experiments were performed for WT and 5 for *cpr5-1*. Mean aniline blue fluorescence intensity was quantified with Fiji using the calloseQuant macro (calloseQuant settings: Method A, peak prominence = 55 and measurement radius = 6) (Huang et al., 2022). Regions of Interest (ROIs) assigned to non-PD regions by the Fiji macro were removed manually. Mean aniline blue fluorescence per image was plotted.

Plasmodesmatal proteome

Preparation of *A. thaliana* plasmodesmatal (PD), cell wall (CW) and total cellular proteins (total cell extract, TC) fractions

Various Arabidopsis shoot tissues, including cauline leaves, meristem, and rosette leaves, were collected individually. Each sample pool consisted of at least six plants. PD preparation involved a minimum of three pools of the same tissue type. Tissues were freshly excised and promptly frozen in liquid nitrogen. The PD preparation protocol was based on two previously published methods (Faulkner and Bayer, 2017; Kraner et al., 2017). Each pool of samples was ground in liquid nitrogen and incubated in PD extraction buffer [150 mM NaCl, 10 mM EDTA, 1 mM DTT, 1% (v/v) Triton X-100, 0.5% (v/v) sodium deoxycholate, 0.1% (w/v) SDS, 10% (v/v) glycerol, and 100 mM Tris-HCl, pH 8] with 0.5% Protease Inhibitor Cocktail (PIC, P9599, Sigma-Aldrich), 5 mM DTT, 1 mM PMSF, 50 mM NaF, 1 mM Na_3VO_4, 1 mM benzamidin and 4 µM leupeptin. For the cell wall fractions, two rounds of grinding in liquid nitrogen efficiently removed soluble protein contaminants and better prepared cell walls for digestion. The pellet was washed at least four times with a low concentration of detergents [150 mM NaCl, 10 mM EDTA, 0.1% (v/v) Triton X-100, 10% (v/v) glycerol, and 100 mM Tris–HCl, pH 8]. After the last washing step, the sample was centrifugated at 1500 x g at 4 °C with swing-out bucket (Sigma 3-30KS, Rotor 11390 & 13150). Cell wall fractions (CW; 100-200 µl) were collected from the final pellet. The rest of the CW pellet was digested in cell wall digestion buffer (1.4% cellulase, mannitol 300mM, 10 mM $CaCl_2$, 10 mM KCl) with 1 mM DTT and 0.5% PIC (P9599, Sigma-Aldrich) at room temperature for 1 h. After centrifugation, the supernatant was collected and ultracentrifuged for 80 min at 4 °C and 110,000 x g (Beckman XPN-80, Rotor SW41Ti). After ultracentrifugation, the resulting pellet was washed twice with TBS buffer (2.5 mM KCl, 140 mM NaCl and 20 mM Tris-HCl, pH 7.4 with 0.5% PIC). The final pellet was PD fraction (PD). Total protein (total cell extract, TC) was extracted according to He *et al*. (He et al., 2022). All fractions were dissolved in 8M UTU (6 M urea, 2 M thiourea, Tris-HCl pH 8.0) before in-solution tryptic digestion.

Protein clean-up, trypsin digestion and peptide desalting

A single-pot, solid-phase-enhanced, sample-preparation (SP3) technology (Hughes et al., 2019) with trypsin digestion was used to remove the detergent in the protein extracts. Disulfide bridges were reduced by an excess of DTT (6.5 mM), and alkylation of free cysteines was done by iodoacetamide (27 mM). SpeedBead Magnetic Carboxylate Modified Particles (SP3 beads, 45152105050250 / 65152105050250, GE Healthcare) were pre-washed by Milli-Q water. SP3 beads (50 µg/µl) were added to the protein sample in a ratio of 1:10. 50% ethanol was used for inducing protein-bead binding. After incubating 15 min at 24 °C, 1,000 rpm constant shaking, the beads were washed three times with 80% ethanol and subjected to trypsin digestion [100 mM Ammonium bicarbonate, trypsin (trypsin: protein ratio 1:100, V5113, Promega)] for 12-14 h at 37 °C. Digested proteins were acidified to pH 2 using TFA and were then desalted over C18 STAGE tips (Rappsilber et al., 2003).

LC-MS/MS analysis of peptides

Peptide mixtures were analyzed by HPLC system nanoflow Easy-nLC (Thermo Scientific, Waltham, Massachusetts) and Orbitrap hybrid mass spectrometer (Q-exactive, Thermo Scientific). Peptides were eluted from a 75 µm x 25 cm analytical C18 column (PepMan, Thermo Scientific) on a linear gradient

running from 5% to 90% acetonitrile over 70 min. Proteins were identified based on the information-dependent acquisition of fragmentation spectra of multiple charged peptides. Up to ten data-dependent MS/MS spectra were acquired in the linear ion trap for each full-scan spectrum acquired at 60,000 full-width half-maximum (FWHM) resolution.

Peptide and protein identification

MaxQuant version 2.2.0.0 was used for raw file peak extraction and protein identification against the Arabidopsis TAIR11 database (35,386 entries). The following parameters were applied: trypsin as cleaving enzyme; minimum peptide length of six amino acids; maximal two missed cleavages; carbamidomethylation of cysteine as a fixed modification; N-terminal protein acetylation, and oxidation of methionine as variable modifications. Peptide mass tolerance was set to 20 ppm, and 0.5 Da was used as the MS/MS tolerance. Multiplicity was set to 1. For label-free quantification, retention time matching between runs was chosen within a time window of two minutes. iBAQ quantification was selected within label-free quantification. The peptide false discovery rate (FDR) and the protein FDR were set to 0.01, while site FDR was set to 0.05. Hits to contaminants (e.g. keratins) and reverse hits identified by MaxQuant were excluded from further analysis. The mass spectrometry proteomics data have been deposited to the ProteomeXchange Consortium via the PRIDE partner repository (Deutsch et al., 2020) with the dataset identifier PXD049466.

PD score (V1.5)

The PD scoring (v1.5) was derived from the earlier PD score equation by Gombos *et al.* (Gombos et al., 2023) with the modification that its components enrichment score and feature score were scaled between 0 and 1. The proteingroups.txt output from Maxquant was analyzed using Perseus. Protein iBAQ values were normalized using z-scores, and the values for PD, CW, and TC fractions were averaged across tissues (file S3). The ratios PD/CW and PD/TC were then calculated based on the average values obtained for each fraction. The PD enrichment score for each protein is the sum of PD/CW and PD/TC. The score was then scaled to a range of 0 to 1, based on the proportion of the distance to the minimum score. Regardless of the enrichment score, the feature score relies on the frequency of protein functions, sublocalizations and PFAM domains (available at https://pfam.xfam.org/) identified within the high-confidence dataset and validated PD candidates (Gombos et al., 2023; Johnston et al., 2023; Kirk et al., 2022). Similar to the enrichment score, the feature score was also normalized to a scale from 0 to 1, based on the proportion of the distance to the minimum score across all *Arabidopsis* proteins (30843 entries). For each protein, the PD score (v 1.5) is obtained by summing the transformed PD enrichment score and the feature score, resulting in a range from 0 to 2. A higher PD score (1.5) indicates a greater likelihood that the protein is a PD protein.

<u>Intercellular Transport assays</u>

Microparticle bombardment

To test passive diffusion of 2xEGFP, microparticle bombardment was performed to deliver DNA coated gold microcarriers into single epidermal cells. 60 mg of 1.0 µm gold microcarriers (Bio-Rad Laboratories, Hercules, CA, USA) were added into a 1.5-mL microcentrifuge tube and washed with 70% ethanol before use. After the final washing step, 1 mL of 50% glycerol was added, and the tube was sealed using Parafilm® (Amcor). The suspended gold particles (35 µL) were labelled with 2 – 2.5 µg of plasmid DNA (pGWB502-p35S:2xmEGFP) in the presence of 0.1 M spermidine and 2.5 M $CaCl_2$. Tubes were vortexed for 1 min and put on ice for 1 min. Coated gold particles were centrifuged at 1,500 x g for 30 sec. The particles were washed twice with 70% ethanol. After the second washing step, 35 µL of 100% ethanol was added and vortexed until the pellet completely dispersed. This gold suspension (10 µL) was transferred onto a macrocarrier (Bio-Rad Laboratories, Hercules, CA, USA). Bombardment was performed using the PDS-1000/He Biolistic Particle Delivery System (Bio-Rad, #1652257) as described (Tee et al., 2022). To visualize bombardments, 2xmEGFP was excited with a 488-nm laser and emission detected at 495-548 nm, while 3xmCherry was excited with a 561-nm laser and emission detected at 548-617 nm. Cells showing fluorescence in the GFP channel were counted manually on maximum projections. To identify the initially bombarded cell, Arabidopsis leaves were bombarded with gold particles coated with pGWB502-p35S:3xmCherry (84 kDa, unable to move passively through non-specific trafficking)

and pGWB502-p35S:2xmEGFP. Fluorescence intensity profile plots across transects were generated using Fiji software package (Schindelin et al., 2012) to analyze the correlation of the fluorescence intensity of mCherry (bombarded cell) and mEGFP (Figure 5-figure supplement 1).

SHR-GFP endodermis-to-stele ratio and Fluorescence Recovery After Photobleaching (FRAP) analysis

SHR–GFP was detected in root endodermis and stele using a Zeiss LSM 900 equipped with Airyscan GaAsP-PMT detectors and diode lasers using a C-Apochromat 40x/1.20 W Korr FCS water objective. For quantification of SHR-GFP, a brief Z-stack series of up to 60 sections of short intervals (2.1 µm) around the ROI were captured, and the Sum-Projection of the volume was analyzed using ImageJ. The background fluorescence was subtracted from the average pixel intensity in the circled region in the endodermis (E) and from the average pixel intensity of the corresponding boxed region in the stele (S) (see Figure 5D). The ratio between endodermis and corresponding stele region was calculated (E:S). Multiple samples were taken for each root to determine the average ratio.

The SHR–GFP fluorescence was bleached in endodermal cells using the 488 nm laser at full laser power for 150 iterations, which lead to around 50-70% reduction in fluorescence. 1-3 cells in the same cell layer were bleached at the same time for each root. To acquire recovery images, laser power was set to 2% to avoid bleaching. The recovery images of the bleached areas were captured every 20 min to reduce the possibility of additional bleaching from frequent scanning. To ensure the identification of the same region of interest during the time-course imaging, a brief Z-stack series of up to 60 sections with short interval (2.1µm) around the region of interest were captured. In this way, the same region should be included in the series of images and can be re-tracked later for analysis. For each time point the Sum-Projection of the same volume was analyzed. The background subtracted fluorescence intensity ratio (endodermis bleached nucleus/endodermis control nucleus) before bleach, after bleach and after 60 minutes was determined using ImageJ (see also Figure 5-figure supplement 1F for positions of ROIs). Time 0 post-bleach fluorescence was set to 0 and all measurements were normalized to this point by subtracting the time 0 post-bleach fluorescence signal from all of the pre-bleach and the recovery values. The percent recovery was calculated using the normalized values. For analysis of intracellular FRAP, a frame size of 512 × 512 pixels with a scanning speed of 0.93 ms per frame (1 Hz) and bi-directional scanning was used to accelerate the scanning rate for each frame.

DANS assay

For Drop-ANd-See (DANS) assays, 1 µl of 10 mM 5-(and 6)-carboxy-fluoresceindiacetat-acetoxymethylester (CFDA) in 0.002 % Silwet® was pipetted on the adaxial side of a rosette leaf and removed after 5 min. The 4th and 24 h later also the 5th rosette leaf was used. For microscopy, the leaf was cut off, washed in water, and mounted between two cover slips. Fluorescence was observed under an Axio Zoom.V16 (Zeiss Microscopy GmbH, Oberkochen, Germany) equipped with a X-Cite Xylts (Excelitas Technologies, PA, USA) LED light source, using a GFP broad bandpass filter cube (excitation: 470/40 nm, beam splitter: FT495 nm, emission: 525/50 nm). Images of the adaxial- and abaxial side were taken using Orca-fusionBT digital camera (C15440, Hamamatsu, Japan). Imaging parameters were consistent across experiments. To identify the fluorescent area, thresholding was performed in ImageJ with the same threshold value for adaxial-and abaxial sides. The diffusion is quantified by ratio between the area above the intensity threshold on the abaxial side and the adaxial side. Experiments of the same day were normalized to the WT experiments of the same day.

<u>Bioinformatics</u>

FG repeat analysis

To identify FG repeat proteins, *A. thaliana* and *P. patens* peptides encoded by gene models were downloaded from Araport 11 and Phypa_V3 genomes and screened, respectively. FG occurrences were counted in a sliding window of 200 amino acids (aa), and the maximum number of FG repeats per window was determined using a custom python script (Supplementary Script 1 and 2). Within the same script, the number of GLFG and xFxFG motifs in each peptide were counted (table S1).

PD index quantification

Overlay of fluorescence from NUP-FPs and aniline blue was quantitatively scored using the PD index (Grison et al., 2019). To minimize bias in quantification, we employed our recently developed PD index script (Gombos et al., 2023). Briefly, clear PD sites were cropped, and channels were separated. PD were identified using auto threshold and Fiji YEN-algorithm, with user modifications. Center coordinates of PD were determined, and square ROIs were set. The PD index was calculated by dividing mean intensity values of PD ROIs by background ROI values. Background ROIs were defined as areas of weak aniline blue fluorescence. Regions previously recognized as PD were automatically omitted from the positioning of background ROIs. Image processing was used for background ROI placement. The software Igor Pro (version 9) was used for data plotting and SPSS was used for statistical analyses.

Structure prediction for CPR5

The structure of CPR5 was predicted using Alphafold monomer version 2.3.1 (Jumper et al., 2021).

Phylogenetic analyses

The tree shown in Figure 4-figure supplement 2 was generated from 68 amino acid sequences as listed in table S7. Full-length sequences were imported into the Molecular Evolutionary Genetics Analysis (MEGA) package version 11, and aligned by CLUSTALW (Tamura et al., 2021). All positions with at least 85% site coverage were used. Phylogenetic analyses were conducted using the Maximum Likelihood method. Based on the suggestions of the "find best protein model (ML)" tool in MEGA 11, the lower BIC (Bayesian Information Criterion) model was selected, which was the JTT matrix-based model (Jones et al., 1992). A discrete Gamma distribution was used to model evolutionary rate differences among sites (five categories, +G, parameter = 6.413). Initial trees for the heuristic search were obtained automatically by applying Neighbor-Joining and BioNJ algorithms to a matrix of pairwise distances estimated using the JTT model, and then selecting the topology with a superior log likelihood value. The bootstrap consensus tree inferred from 1000 replicates was taken to represent the evolutionary history of the analyzed genes. Branches corresponding to partitions reproduced in less than 50% bootstrap replicates were collapsed.

Statistics

In the PD proteome from Arabidopsis leaf tissue, we identified 5145 proteins from PD, CW, and TC fractions, with 3347 proteins having a PD score > 0.63. Among them, 3062 proteins were quantifiable in the PD fraction, constituting our Arabidopsis shoot PD proteome. Among these, 2268 proteins were categorized as high-confidence PD proteins, while 792 proteins fall into the medium-confidence category (file S3). The PD index is based on the analysis of at least 15 images from three independent repeats for each NUP and negative control. The quantification of the intercellular spread of 2xmEGFP by counting fluorescent cells in the mEGFP channel is based on the analysis of $n_{(WT)} = 17$ independent biological experiments with in total 594 bombarded cells; $n_{(cpr5\text{-}1)} = 6$ independent biological replicates with in total 278 bombarded cells; $n_{(cpr5\text{-}T3)} = 4$ independent biological replicates with in total 99 bombarded cells. Kruskal-Wallis test with Bonferroni correction for pairwise comparison was used to test for significant differences in mean cell counts between WT, *cpr5-1*, and *cpr5-T3* with $p_{(WT\ vs.\ cpr5\text{-}1)} < 1x10^{-10}$, $p_{(WT\ vs.\ cpr5\text{-}T3)} = 0.025$, and $p_{(cpr5\text{-}1\ vs.\ cpr5\text{-}T3)} = 0.00005$. The *p*-values are summarized in table S2. The callose quantification is based on $n_{(WT)} = 4$ independent experiments, $n_{(cpr5\text{-}1)} = 5$ independent experiments. Student´s *t*-test indicated a non-significant difference with $p = 0.48$.

SHR-GFP endodermis-to-stele ratio is based on the quantification of $n_{(WT)} = 62$ and $n_{(cpr5\text{-}1)} = 62$ different endodermis nuclei and corresponding stele regions, while per root 3-4 different nuclei and corresponding stele regions were quantified. For endodermis-to-stele ratio, Mann-Whitney U test indicated a significant difference between WT and *cpr5-1* background with $p = 0.0006$. For baseline stele fluorescence, Mann-Whitney U test indicated no significant differences between s*hr* and s*hr x cpr5-1* with $p = 0.074$. The quantification of SHR-GFP fluorescence recovery was normalized to a control nucleus in the endodermis (see Methods and Figure 5-figure supplement 1F) and is based on n(WT) = 59 and n(*cpr5-1*) = 59 bleached nuclei, while per root 3-4 nuclei were bleached. Student´s T-Test indicated a significant difference between WT and *cpr5-1* background with p = 0.037.

For the DANS data, Kruskal-Wallis test with Bonferroni correction for pairwise comparison was used to test for significant differences between WT and mutant lines. All statistical test were performed with SPSS. In all box plots median is represented by vertical line inside the box, mean is represented by the

bold +. Values between quartiles 1 and 3 are represented by box ranges, and 5th and 95th percentile are represented by error bars. Data was plotted using Igor Pro (version 9).

References

Alazem M, Nuzzi SN, Burch-Smith TM. 2025. Viral Movement Proteins and Plasmodesmata: turning gatekeepers into gateways. *J Exp Bot* eraf184. doi:10.1093/jxb/eraf184

Apelt L, Knockenhauer KE, Leksa NC, Benlasfer N, Schwartz TU, Stelzl U. 2016. Systematic protein–protein interaction analysis reveals intersubcomplex contacts in the Nuclear Pore Complex. *Mol Cell Proteomics MCP* **15**:2594–2606. doi:10.1074/mcp.M115.054627

Arra Y, Auguy F, Stiebner M, Chéron S, Wudick MM, Miras M, Schepler-Luu V, Köhler S, Cunnac S, Frommer WB, Albar L. 2024. Rice Yellow Mottle Virus resistance by genome editing of the *Oryza sativa L. ssp. japonica* nucleoporin gene *OsCPR5.1* but not *OsCPR5.2*. *Plant Biotechnol J* **22**:1299–1311. doi:10.1111/pbi.14266

Ascencio-Ibanez JT, Sozzani R, Lee TJ, Chu TM, Wolfinger RD, Cella R, Hanley-Bowdoin L. 2008. Global analysis of Arabidopsis gene expression uncovers a complex array of changes impacting pathogen response and cell cycle during geminivirus infection. *Plant Physiol* **148**:436–54. doi:10.1104/pp.108.121038

Bayer EM, Bottrill AR, Walshaw J, Vigouroux M, Naldrett MJ, Thomas CL, Maule AJ. 2006. Arabidopsis cell wall proteome defined using multidimensional protein identification technology. *Proteomics* **6**:301–311. doi:10.1002/pmic.200500046

Blasius TL, Takao D, Verhey KJ. 2019. NPHP proteins are binding partners of nucleoporins at the base of the primary cilium. *PLOS ONE* **14**:e0222924. doi:10.1371/journal.pone.0222924

Bleckmann A, Weidtkamp-Peters S, Seidel CA, Simon R. 2010. Stem cell signaling in Arabidopsis requires CRN to localize CLV2 to the plasma membrane. *Plant Physiol* **152**:166–76. doi:10.1104/pp.109.149930

Bowling SA, Clarke JD, Liu Y, Klessig DF, Dong X. 1997. The cpr5 mutant of Arabidopsis expresses both NPR1-dependent and NPR1-independent resistance. *Plant Cell* **9**:1573–84.

Bowling SA, Guo A, Cao H, Gordon AS, Klessig DF, Dong X. 1994. A mutation in Arabidopsis that leads to constitutive expression of systemic acquired resistance. *Plant Cell* **6**:1845–5187.

Brault ML, Petit JD, Immel F, Nicolas WJ, Glavier M, Brocard L, Gaston A, Fouché M, Hawkins TJ, Crowet J-M, Grison MS, Germain V, Rocher M, Kraner M, Alva V, Claverol S, Paterlini A, Helariutta Y, Deleu M, Lins L, Tilsner J, Bayer EM. 2019. Multiple C2 domains and transmembrane region proteins (MCTPs) tether membranes at plasmodesmata. *EMBO Rep* **20**:e47182. doi:10.15252/embr.201847182

Campbell R, Cowan G, Wurzinger B, Ducreux LJM, Dessoly J, Guo W, Zhang R, Morris JA, Hedley P, Wahl V, Taylor MA, Hancock RD. 2025. GERMIN3 regulates tuber initiation and axillary bud activation by facilitating plasmodesmatal gating. *Plant J* **122**:e70186. doi:10.1111/tpj.70186

Chen C-C, Fu S-F, Lee Y-I, Lin C-Y, Lin W-C, Huang H-J. 2012. Transcriptome analysis of age-related gain of callus-forming Capacity in Arabidopsis hypocotyls. *Plant Cell Physiol* **53**:1457–1469. doi:10.1093/pcp/pcs090

Chen G, Xu D, Liu Q, Yue Z, Dai B, Pan S, Chen Y, Feng X, Hu H. 2023. Regulation of FLC nuclear import by coordinated action of the NUP62-subcomplex and importin β SAD2. *J Integr Plant Biol* **65**:2086–2106. doi:10.1111/jipb.13540

Chopra K, Bawaria S, Chauhan R. 2019. Evolutionary divergence of the nuclear pore complex from fungi to metazoans. *Protein Sci* **28**:571–586. doi:10.1002/pro.3558

Collins PP, Broad RC, Yogeeswaran K, Varsani A, Poole AM, Collings DA. 2023. Characterisation of the trans-membrane nucleoporins GP210 and NDC1 in *Arabidopsis thaliana*. *Plant Sci* **332**:111719. doi:10.1016/j.plantsci.2023.111719

Craige B, Tsao C-C, Diener DR, Hou Y, Lechtreck K-F, Rosenbaum JL, Witman GB. 2010. CEP290 tethers flagellar transition zone microtubules to the membrane and regulates flagellar protein content. *J Cell Biol* **190**:927–940. doi:10.1083/jcb.201006105

Crawford KM, Zambryski PC. 2001. Non-targeted and targeted protein movement through plasmodesmata in leaves in different developmental and physiological states. *Plant Physiol* **125**:1802–1812.

Crawford KM, Zambryski PC. 2000. Subcellular localization determines the availability of non-targeted proteins to plasmodesmatal transport. *Curr Biol* **10**:1032–1040. doi:10.1016/S0960-9822(00)00657-6

Cui H, Levesque MP, Vernoux T, Jung JW, Paquette AJ, Gallagher KL, Wang JY, Blilou I, Scheres B, Benfey PN. 2007. An evolutionarily conserved mechanism delimiting SHR movement defines a single layer of endodermis in plants. *Science* **316**:421–5. doi:10.1126/science.1139531

del Viso F, Huang F, Myers J, Chalfant M, Zhang Y, Reza N, Bewersdorf J, Lusk CP, Khokha MK. 2016. Congenital heart disease genetics uncovers context-dependent organization and function of nucleoporins at cilia. *Dev Cell* **38**:478–492. doi:10.1016/j.devcel.2016.08.002

Deutsch EW, Bandeira N, Sharma V, Perez-Riverol Y, Carver JJ, Kundu DJ, García-Seisdedos D, Jarnuczak AF, Hewapathirana S, Pullman BS, Wertz J, Sun Z, Kawano S, Okuda S, Watanabe Y, Hermjakob H, MacLean B, MacCoss MJ, Zhu Y, Ishihama Y, Vizcaíno JA. 2020. The ProteomeXchange consortium in 2020: enabling "big data" approaches in proteomics. *Nucleic Acids Res* **48**:D1145–D1152. doi:10.1093/nar/gkz984

Dickmanns M, Pöge M, Xu P, Gombos S, Miras M, Plitzko JM, Simon R, Schulze WX, Frommer WB, Baumeister W. 2025. *In situ* architecture of plasmodesmata suggests mechanisms controlling intercellular exchange. *bioRxiv*.

Dyachok J, Yoo C-M, Palanichelvam K, Blancaflor EB. 2010. Sample preparation for fluorescence imaging of the cytoskeleton in fixed and living plant roots In: Gavin RH, editor. Cytoskeleton Methods and Protocols, Methods in Molecular Biology. Totowa, NJ: Humana Press. pp. 157–169. doi:10.1007/978-1-60761-376-3_8

Ejike JO, Davis GV, Restrepo-Escobar A, Dalal A, Nakamura M, Frommer WB, Schladt TM. 2025. The role of phase separation for RNA and protein transport through the nuclear pore complex. *J Exp Bot* eraf271. doi:10.1093/jxb/eraf271

Epting D, Decker E, Ott E, Eisenberger T, Bader I, Bachmann N, Bergmann C. 2022. The ciliary transition zone protein TMEM218 synergistically interacts with the NPHP module and its reduced dosage leads to a wide range of syndromic ciliopathies. *Hum Mol Genet* **31**:2295–2306. doi:10.1093/hmg/ddac027

Faulkner C, Akman OE, Bell K, Jeffree C, Oparka K. 2008. Peeking into pit fields: a multiple twinning model of secondary plasmodesmata formation in tobacco. *Plant Cell* **20**:1504–1518. doi:10.1105/tpc.107.056903

Faulkner C, Bayer EM. 2017. Isolation of plasmodesmata. *Methods Mol Biol* **1511**:187–198. doi:10.1007/978-1-4939-6533-5_15

Faulkner C, Petutschnig E, Benitez-Alfonso Y, Beck M, Robatzek S, Lipka V, Maule AJ. 2013. LYM2-dependent chitin perception limits molecular flux via plasmodesmata. *Proc Natl Acad Sci* **110**:9166–9170. doi:10.1073/pnas.1203458110

Fernandez-Calvino L, Faulkner C, Walshaw J, Saalbach G, Bayer EM, Benitez-Alfonso Y, Maule AJ. 2011. Arabidopsis plasmodesmal proteome. *PloS One* **6**:e18880. doi:10.1371/journal.pone.0018880

Fitzgibbon J, Bell K, King E, Oparka K. 2010. Super-resolution imaging of plasmodesmata using three-dimensional structured illumination microscopy. *Plant Physiol* **153**:1453–63. doi:10.1104/pp.110.157941

Frey S, Rees R, Schünemann J, Ng SC, Fünfgeld K, Huyton T, Görlich D. 2018. Surface properties determining passage rates of proteins through nuclear pores. *Cell* **174**:202-217.e9. doi:10.1016/j.cell.2018.05.045

Gadella TWJ, van Weeren L, Stouthamer J, Hink MA, Wolters AHG, Giepmans BNG, Aumonier S, Dupuy J, Royant A. 2023. mScarlet3: a brilliant and fast-maturing red fluorescent protein. *Nat Methods* **20**:541–545. doi:10.1038/s41592-023-01809-y

Gallemí M, Galstyan A, Paulišić S, Then C, Ferrández-Ayela A, Lorenzo-Orts L, Roig-Villanova I, Wang X, Micol JL, Ponce MR, Devlin PF, Martínez-García JF. 2016. DRACULA2 is a dynamic nucleoporin with a role in regulating the shade avoidance syndrome in Arabidopsis. *Development* **143**:1623–1631. doi:10.1242/dev.130211

Giordano F, Saheki Y, Idevall-Hagren O, Colombo SF, Pirruccello M, Milosevic I, Gracheva EO, Bagriantsev SN, Borgese N, De Camilli P. 2013. PI(4,5)P_2-dependent and Ca^{2+}-regulated ER-PM interactions mediated by the extended synaptotagmins. *Cell* **153**:1494–1509. doi:10.1016/j.cell.2013.05.026

Gombos S, Miras M, Howe V, Xi L, Pottier M, Kazemein Jasemi NS, Schladt M, Ejike JO, Neumann U, Hänsch S, Kuttig F, Zhang Z, Dickmanns M, Xu P, Stefan T, Baumeister W, Frommer WB, Simon R, Schulze WX. 2023. A high-confidence *Physcomitrium patens* plasmodesmata proteome by iterative scoring and validation reveals diversification of cell wall proteins during evolution. *New Phytol* **238**:637–653. doi:10.1111/nph.18730

Grison MS, Kirk P, Brault ML, Wu XN, Schulze WX, Benitez-Alfonso Y, Immel F, Bayer EM. 2019. Plasma membrane-associated receptor-like kinases relocalize to plasmodesmata in response to osmotic stress. *Plant Physiol* **181**:142–160. doi:10.1104/pp.19.00473

Gu Y, Zebell SG, Liang Z, Wang S, Kang B-H, Dong X. 2016. Nuclear pore permeabilization is a convergent signaling event in effector-triggered immunity. *Cell* **166**:1526-1538.e11. doi:10.1016/j.cell.2016.07.042

He M, Wang J, Herold S, Xi L, Schulze WX. 2022. A rapid and universal workflow for label-free-quantitation-based proteomic and phosphoproteomic studies in cereals. *Curr Protoc* **2**:e425. doi:10.1002/cpz1.425

Hodel AE, Hodel MR, Griffis ER, Hennig KA, Ratner GA, Xu S, Powers MA. 2002. The three-dimensional structure of the autoproteolytic, nuclear pore-targeting domain of the human nucleoporin Nup98. *Mol Cell* **10**:347–358. doi:10.1016/S1097-2765(02)00589-0

Hoogenboom BW, Hough LE, Lemke EA, Lim RYH, Onck PR, Zilman A. 2021. Physics of the nuclear pore complex: Theory, modeling and experiment. *Phys Rep* **921**:1–53. doi:10.1016/j.physrep.2021.03.003

Howell AH, Christensen AH, James V, Vasina VV, Jensen KH, Foley J, Evans JE, Stone HA, Peters WS, Knoblauch M. 2024. Electric charge controls plasmodesma conductivity. doi:10.1101/2024.04.02.587779

Huang C, Mutterer J, Heinlein M. 2022. In vivo aniline blue staining and semiautomated quantification of callose deposition at plasmodesmata In: Benitez-Alfonso Y, Heinlein M, editors. Plasmodesmata: Methods and Protocols, Methods in Molecular Biology. New York, NY: Springer US. pp. 151–165. doi:10.1007/978-1-0716-2132-5_9

Hughes CS, Moggridge S, Müller T, Sorensen PH, Morin GB, Krijgsveld J. 2019. Single-pot, solid-phase-enhanced sample preparation for proteomics experiments. *Nat Protoc* **14**:68–85. doi:10.1038/s41596-018-0082-x

Johnson CA, Malicki JJ. 2019. The nuclear arsenal of cilia. *Dev Cell* **49**:161–170. doi:10.1016/j.devcel.2019.03.009

Johnston MG, Breakspear A, Samwald S, Zhang D, Papp D, Faulkner C, de Keijzer J. 2023. Comparative phyloproteomics identifies conserved plasmodesmal proteins. *J Exp Bot* **74**:1821–1835. doi:10.1093/jxb/erad022

Jones DT, Taylor WR, Thornton JM. 1992. The rapid generation of mutation data matrices from protein sequences. *Bioinformatics* **8**:275–282. doi:10.1093/bioinformatics/8.3.275

Jumper J, Evans R, Pritzel A, Green T, Figurnov M, Ronneberger O, Tunyasuvunakool K, Bates R, Žídek A, Potapenko A, Bridgland A, Meyer C, Kohl SAA, Ballard AJ, Cowie A, Romera-Paredes B, Nikolov S, Jain R, Adler J, Back T, Petersen S, Reiman D, Clancy E, Zielinski M, Steinegger M, Pacholska M, Berghammer T, Bodenstein S, Silver D, Vinyals O, Senior AW, Kavukcuoglu K, Kohli P, Hassabis D. 2021. Highly accurate protein structure prediction with AlphaFold. *Nature* **596**:583–589. doi:10.1038/s41586-021-03819-2

Kehlenbach RH, Neumann P, Ficner R, Dickmanns A. 2023. Interaction of nucleoporins with nuclear transport receptors: a structural perspective. *Biol Chem* **404**:791–805. doi:10.1515/hsz-2023-0155

Kessel RG. 1992. Annulate lamellae: a last frontier in cellular organelles In: Jeon KW, Friedlander M, editors. Int. Rev. Cytol. Academic Press. pp. 43–120. doi:10.1016/S0074-7696(08)61858-6

Kirk P, Amsbury S, German L, Gaudioso-Pedraza R, Benitez-Alfonso Y. 2022. A comparative meta-proteomic pipeline for the identification of plasmodesmata proteins and regulatory conditions in diverse plant species. *BMC Biol* **20**:128. doi:10.1186/s12915-022-01331-1

Kohler A, Schwindling S, Conrath U. 2002. Benzothiadiazole-induced priming for potentiated responses to pathogen infection, wounding, and infiltration of water into leaves requires the *NPR1/NIM1* gene in Arabidopsis. *Plant Physiol* **128**:1046–1056. doi:10.1104/pp.010744

Koizumi K, Hayashi T, Wu S, Gallagher KL. 2012. The SHORT-ROOT protein acts as a mobile, dose-dependent signal in patterning the ground tissue. *Proc Natl Acad Sci U S A* **109**:13010–13015. doi:10.1073/pnas.1205579109

Kragler F, Monzer J, Shash K, Xoconostle-Cázares B, Lucas WJ. 1998. Cell-to-cell transport of proteins: Requirement for unfolding and characterization of binding to a putative plasmodesmal receptor. *Plant J* **15**:367–381. doi:10.1046/j.1365-313X.1998.00219.x

Kraner ME, Müller C, Sonnewald U. 2017. Comparative proteomic profiling of the choline transporter-like1 (CHER1) mutant provides insights into plasmodesmata composition of fully developed *Arabidopsis thaliana* leaves. *Plant J Cell Mol Biol* **92**:696–709. doi:10.1111/tpj.13702

Lampropoulos A, Sutikovic Z, Wenzl C, Maegele I, Lohmann JU, Forner J. 2013. GreenGate - a novel, versatile, and efficient cloning system for plant transgenesis. *PLOS ONE* **8**:e83043. doi:10.1371/journal.pone.0083043

Lee H, Xiong L, Gong Z, Ishitani M, Stevenson B, Zhu J-K. 2001. The Arabidopsis HOS1 gene negatively regulates cold signal transduction and encodes a RING finger protein that displays cold-regulated nucleo–cytoplasmic partitioning. *Genes Dev* **15**:912–924. doi:10.1101/gad.866801

Lee JH, Kim JJ, Kim SH, Cho HJ, Kim J, Ahn JH. 2012. The E3 ubiquitin ligase HOS1 regulates low ambient temperature-responsive flowering in *Arabidopsis thaliana*. *Plant Cell Physiol* **53**:1802–1814. doi:10.1093/pcp/pcs123

Lee J-Y, Wang X, Cui W, Sager R, Modla S, Czymmek K, Zybaliov B, van Wijk K, Zhang C, Lu H, Lakshmanan V. 2011. A plasmodesmata-localized protein mediates crosstalk between cell-to-cell communication and innate immunity in Arabidopsis. *Plant Cell* **23**:3353–3373. doi:10.1105/tpc.111.087742

Lee JY, Yoo BC, Lucas WJ. 2000. Parallels between nuclear-pore and plasmodesmal trafficking of information molecules. *Planta* **210**:177–187.

Lee J-Y, Yoo B-C, Rojas MR, Gomez-Ospina N, Staehelin LA, Lucas WJ. 2003. Selective trafficking of non-cell-autonomous proteins mediated by NtNCAPP1. *Science* **299**:392–396. doi:10.1126/science.1077813

Li C, Jensen VL, Park K, Kennedy J, Garcia-Gonzalo FR, Romani M, Mori RD, Bruel A-L, Gaillard D, Doray B, Lopez E, Rivière J-B, Faivre L, Thauvin-Robinet C, Reiter JF, Blacque OE, Valente EM, Leroux MR. 2016. MKS5 and CEP290 dependent assembly pathway of the ciliary transition zone. *PLOS Biol* **14**:e1002416. doi:10.1371/journal.pbio.1002416

Li Z, Liu S-L, Montes-Serey C, Walley JW, Aung K. 2024. PLASMODESMATA-LOCATED PROTEIN 6 regulates plasmodesmal function in Arabidopsis vasculature. *Plant Cell* **36**:3543–3561. doi:10.1093/plcell/koae166

Lin DH, Hoelz A. 2019. The structure of the nuclear pore complex (an update). *Annu Rev Biochem* **88**:725–783. doi:10.1146/annurev-biochem-062917-011901

Lu H, Ge P, Ma Y, Lin F, Jing D, Zhou T, Cui F. 2025. Loss-of-function of two PD-associated proteins confers resistance to rice stripe virus. *Mol Plant Pathol* **26**:e70121. doi:10.1111/mpp.70121

Ma M, Li M, Zhou R, Yu J-B, Wu Y, Zhang X, Wang J, Zhou J-M, Liang X. 2023. CPR5 positively regulates pattern-triggered immunity via a mediator protein. *J Integr Plant Biol* **65**:1613–1619. doi:10.1111/jipb.13472

Makarov AA, Padilla-Mejia NE, Field MC. 2021. Evolution and diversification of the nuclear pore complex. *Biochem Soc Trans* **49**:1601–1619. doi:10.1042/BST20200570

Mansfeld J, Güttinger S, Hawryluk-Gara LA, Panté N, Mall M, Galy V, Haselmann U, Mühlhäusser P, Wozniak RW, Mattaj IW, Kutay U, Antonin W. 2006. The conserved transmembrane nucleoporin NDC1 is required for nuclear pore complex assembly in vertebrate cells. *Mol Cell* **22**:93–103. doi:10.1016/j.molcel.2006.02.015

Miyashima S, Koi S, Hashimoto T, Nakajima K. 2011. Non-cell-autonomous microRNA165 acts in a dose-dependent manner to regulate multiple differentiation status in the Arabidopsis root. *Development* **138**:2303–2313. doi:10.1242/dev.060491

Mosalaganti S, Obarska-Kosinska A, Siggel M, Taniguchi R, Turoňová B, Zimmerli CE, Buczak K, Schmidt FH, Margiotta E, Mackmull M-T, Hagen WJH, Hummer G, Kosinski J, Beck M. 2022. AI-based structure prediction empowers integrative structural analysis of human nuclear pores. *Science* **376**:eabm9506. doi:10.1126/science.abm9506

Nakajima K, Sena G, Nawy T, Benfey PN. 2001. Intercellular movement of the putative transcription factor SHR in root patterning. *Nature* **413**:307–311. doi:10.1038/35095061

Narsai R, Law SR, Carrie C, Xu L, Whelan J. 2011. In-depth temporal transcriptome profiling reveals a crucial developmental switch with roles for RNA processing and organelle metabolism that are essential for germination in Arabidopsis. *Plant Physiol* **157**:1342–1362. doi:10.1104/pp.111.183129

Ng SC, Biswas A, Huyton T, Schünemann J, Reber S, Görlich D. 2023. Barrier properties of NUP98 FG phases ruled by FG motif identity and inter-FG spacer length. *Nat Commun* **14**:747–747. doi:10.1038/s41467-023-36331-4

Ng SC, Güttler T, Görlich D. 2021. Recapitulation of selective nuclear import and export with a perfectly repeated 12mer GLFG peptide. *Nat Commun* **12**:4047. doi:10.1038/s41467-021-24292-5

Nicolas WJ, Grison MS, Trépout S, Gaston A, Fouché M, Cordelières FP, Oparka KJ, Tilsner J, Brocard L, Bayer EM. 2017. Architecture and permeability of post-cytokinesis plasmodesmata lacking cytoplasmic sleeves. *Nat Plants* **3**:17082. doi:10.1038/nplants.2017.82

Okuma E, Nozawa R, Murata Y, Miura K. 2014. Accumulation of endogenous salicylic acid confers drought tolerance to Arabidopsis. *Plant Signal Behav* **9**:e28085. doi:10.4161/psb.28085

Otero S, Helariutta Y, Benitez-Alfonso Y. 2016. Symplastic communication in organ formation and tissue patterning. *Curr Opin Plant Biol* **29**:21–28. doi:10.1016/j.pbi.2015.10.007

Paultre DSG, Gustin M-P, Molnar A, Oparka KJ. 2016. Lost in transit: long-distance trafficking and phloem unloading of protein signals in Arabidopsis homografts. *Plant Cell* **28**:2016–2025. doi:10.1105/tpc.16.00249

Pendle A, Benitez-Alfonso Y. 2015. Immunofluorescence detection of callose deposition around plasmodesmata sites. *Methods Mol Biol Clifton NJ* **1217**:95–104. doi:10.1007/978-1-4939-1523-1_6

Peng S, Guo D, Guo Y, Zhao H, Mei J, Han Y, Guan R, Wang T, Song T, Sun K, Liu Y, Mao T, Chang H, Xue J, Cai Y, Chen D, Wang S. 2022. CONSTITUTIVE EXPRESSER of PATHOGENESIS-RELATED GENES 5 is an RNA-binding protein controlling plant immunity via an RNA processing complex. *Plant Cell* **34**:1724–1744. doi:10.1093/plcell/koac037

Penzo A, Palancade B. 2023. Puzzling out nuclear pore complex assembly. *FEBS Lett* **597**:2705–2727. doi:10.1002/1873-3468.14713

Pletan M, Wang E, Gohmann L, Tsai B. 2025. An ER-associated structure sequesters misassembled FG-rich nucleoporins to help maintain nuclear pore complex function. *J Cell Sci* **138**:jcs263659. doi:10.1242/jcs.263659

Pöge M, Dickmanns M, Xu P, Li M, Schiøtz OH, Kaiser CO, Ma J, Bieber A, Capitanio C, Brenner J, Riggi M, Klumpe S, Miras M, Jasemi NSK, Schulze WX, Simon R, Frommer WB, Plitzko JM, Baumeister W. 2025. Making plant tissue accessible for cryo-electron tomography. *eLife* **14**. doi:10.7554/eLife.106455.1

Qu F, Morris TJ. 2002. Efficient infection of *Nicotiana benthamiana* by tomato bushy stunt virus Is facilitated by the coat protein and maintained by p19 through suppression of gene silencing. *Mol Plant-Microbe Interactions®* **15**:193–202. doi:10.1094/MPMI.2002.15.3.193

Rappsilber J, Ishihama Y, Mann M. 2003. Stop and go extraction tips for matrix-assisted laser desorption/ionization, nanoelectrospray, and LC/MS sample pretreatment in proteomics. *Anal Chem* **75**:663–670. doi:10.1021/ac026117i

Ross-Elliott TJ, Jensen KH, Haaning KS, Wager BM, Knoblauch J, Howell AH, Mullendore DL, Monteith AG, Paultre D, Yan D, Otero S, Bourdon M, Sager R, Lee J-Y, Helariutta Y, Knoblauch M, Oparka KJ. 2017. Phloem unloading in Arabidopsis roots is convective and regulated by the phloem-pole pericycle. *eLife* **6**:e24125. doi:10.7554/eLife.24125

Sakulkoo W, Osés-Ruiz M, Oliveira Garcia E, Soanes DM, Littlejohn GR, Hacker C, Correia A, Valent B, Talbot NJ. 2018. A single fungal MAP kinase controls plant cell-to-cell invasion by the rice blast fungus. *Science* **359**:1399–1403. doi:10.1126/science.aaq0892

Scheer U, Franke WW. 1972. Annulate lamellae in plant cells: Formation during microsporogenesis and pollen development in Canna generalis Bailey. *Planta* **107**:145–159. doi:10.1007/BF00387720

Schindelin J, Arganda-Carreras I, Frise E, Kaynig V, Longair M, Pietzsch T, Preibisch S, Rueden C, Saalfeld S, Schmid B, Tinevez JY, White DJ, Hartenstein V, Eliceiri K, Tomancak P, Cardona A. 2012. Fiji: an open-source platform for biological-image analysis. *Nat Methods* **9**:676–82. doi:10.1038/nmeth.2019

Shimada TL, Shimada T, Hara-Nishimura I. 2010. A rapid and non-destructive screenable marker, FAST, for identifying transformed seeds of *Arabidopsis thaliana*. *Plant J* **61**:519–528. doi:10.1111/j.1365-313X.2009.04060.x

Shimozono S, Miyawaki A. 2008. Engineering FRET constructs using CFP and YFPMethods in Cell Biology, Fluorescent Proteins. Academic Press. pp. 381–393. doi:10.1016/S0091-679X(08)85016-9

Song L i, Zhou X-Y, Li L i, Xue L-J, Yang X i, Xue H-W. 2009. Genome-wide analysis revealed the complex regulatory network of brassinosteroid effects in photomorphogenesis. *Mol Plant* **2**:755–772. doi:10.1093/mp/ssp039

Takao D, Wang L, Boss A, Verhey KJ. 2017. Protein interaction analysis provides a map of the spatial and temporal organization of the ciliary gating zone. *Curr Biol* **27**:2296-2306.e3. doi:10.1016/j.cub.2017.06.044

Tamura K, Fukao Y, Iwamoto M, Haraguchi T, Hara-Nishimura I. 2010. Identification and characterization of nuclear pore complex components in *Arabidopsis thaliana*. *Plant Cell* **22**:4084–4097. doi:10.1105/tpc.110.079947

Tamura K, Stecher G, Kumar S. 2021. MEGA11: Molecular Evolutionary Genetics Analysis Version 11. *Mol Biol Evol* **38**:3022–3027. doi:10.1093/molbev/msab120

Tang Y, Huang A, Gu Y. 2020. Global profiling of plant nuclear membrane proteome in Arabidopsis. *Nat Plants* **6**:838–847. doi:10.1038/s41477-020-0700-9

Tee EE, Faulkner C. 2024. Plasmodesmata and intercellular molecular traffic control. *New Phytol* **243**:32–47. doi:10.1111/nph.19666

Tee EE, Samwald S, Faulkner C. 2022. Quantification of cell-to-cell connectivity using particle bombardment. *Methods Mol Biol Clifton NJ* **2457**:263–272. doi:10.1007/978-1-0716-2132-5_17

Terry LJ, Wente SR. 2009. Flexible gates: dynamic topologies and functions for FG nucleoporins in nucleocytoplasmic transport. *Eukaryot Cell* **8**:1814–1827. doi:10.1128/EC.00225-09

Thomas CL, Bayer EM, Ritzenthaler C, Fernandez-Calvino L, Maule AJ. 2008. Specific targeting of a plasmodesmal protein affecting cell-to-cell communication. *PLoS Biol* **6**:e7. doi:10.1371/journal.pbio.0060007

Wang F, Wang L, Qiao L, Chen J, Pappa MB, Pei H, Zhang T, Chang C, Dong C-H. 2017. Arabidopsis CPR5 regulates ethylene signaling via molecular association with the ETR1 receptor. *J Integr Plant Biol* **59**:810–824. doi:10.1111/jipb.12570

Wang S, Gu Y, Zebell SG, Anderson LK, Wang W, Mohan R, Dong X. 2014. A noncanonical role for the CKI-RB-E2F cell-cycle signaling pathway in plant effector-triggered immunity. *Cell Host Microbe* **16**:787–794. doi:10.1016/j.chom.2014.10.005

Winter CM, Szekely P, Popov V, Belcher H, Carter R, Jones M, Fraser SE, Truong TV, Benfey PN. 2024. SHR and SCR coordinate root patterning and growth early in the cell cycle. *Nature* 1–6. doi:10.1038/s41586-023-06971-z

Xiao L, Jiang S, Huang P, Chen F, Wang X, Cheng Z, Miao Y, Liu L, Searle I, Liu C, Wu X-X, Fu Y-F, Chen Q, Zhang X-M. 2020. Two *Nucleoporin98* homologous genes jointly participate in the regulation of starch degradation to repress senescence in Arabidopsis. *BMC Plant Biol* **20**:292. doi:10.1186/s12870-020-02494-1

Xie W, Nielsen ME, Pedersen C, Thordal-Christensen H. 2017. A split-GFP gateway cloning system for topology analyses of membrane proteins in plants. *PLOS ONE* **12**:e0170118. doi:10.1371/journal.pone.0170118

Yu M, Heidari M, Mikhaleva S, Tan PS, Mingu S, Ruan H, Reinkemeier CD, Obarska-Kosinska A, Siggel M, Beck M, Hummer G, Lemke EA. 2023. Visualizing the disordered nuclear transport machinery *in situ*. *Nature* **617**:162–169. doi:10.1038/s41586-023-05990-0

Zavaliev R, Epel BL. 2015. Imaging callose at plasmodesmata using aniline blue: quantitative confocal microscopy. *Methods Mol Biol Clifton NJ* **1217**:105–119. doi:10.1007/978-1-4939-1523-1_7

Zhang C, An N, Jia P, Zhang W, Liang J, Zhang X, Zhou H, Ma W, Han M, Xing L, Ren X. 2020. Genomic identification and expression analysis of nuclear pore proteins in *Malus domestica*. *Sci Rep* **10**:17426. doi:10.1038/s41598-020-74171-0

Zimmerli CE, Allegretti M, Rantos V, Goetz SK, Obarska-Kosinska A, Zagoriy I, Halavatyi A, Hummer G, Mahamid J, Kosinski J, Beck M. 2021. Nuclear pores dilate and constrict *in cellulo*. *Science* **374**:eabd9776. doi:10.1126/science.abd9776

Acknowledgments
We would like to dedicate this manuscript to the 'champion of plasmodesmata', William J. (Bill) Lucas (UC Davis). We thank Madlen Somsich (HHU) for project coordination and management. This work has received funding from the European Research Council (ERC) and the Marie Skłodowska-Curie Actions under the European Union's Horizon 2020 research and innovation program (Grant agreements 'SymPore' No. 951292 to WBF and "PDgate" No. 101023981 to MM, respectively). ARE was supported in part by funds from the Interdisciplinary Graduate and Research Academy (iGRAD) Düsseldorf (Deutsche Forschungsgemeinschaft (DFG, German Research Foundation), DFG, project ID 391465903/GRK 2466). Research was also supported by the Deutsche Forschungsgemeinschaft (DFG, German Research Foundation) under Germany´s Excellence Strategy – EXC-2048/1 – project ID 390686111, and the Alexander von Humboldt Professorship, to WBF.

Data availability

Source data have been assigned a DOI (http://doi.org/10.60534/46qra-6bw98) and are accessible via https://git.nfdi4plants.org/projects/2188. Materials will be made available under MTA; some materials were obtained from others as marked and require permission from the respective authors.

Contributions

WBF conceived of the study. J.E. performed the bioinformatic analyses; L.X., S.G. and W.S. performed proteomics and data analysis; M.D. analyzed the structure and generated Figure 2-figure supplement 1; S.H. helped to establish and advised on SIM. T.M.S, M.P., M.M., J.O.E., N.P., M.N., G.V.D, C.G. and A.D. performed imaging and/or transport studies; R.S. advised on imaging and data analyses; M.M. and A.R-E. performed split GFP studies, T.M.S, M.M., M.P., J.O.E., B.S., and W.B.F. analyzed the data; T.M.S., M.M., M.P., J.O.E., G.V.D, R.S. and W.B.F. wrote the manuscript.

Competing interests

We declare no competing interests.

Supplementary Materials

- 8 Supplementary Tables
- 9 Supplementary Figures
- 3 Supplementary files
- 2 Supplemental scripts

Figures with supplements and legends

Figure 1 with 3 supplements

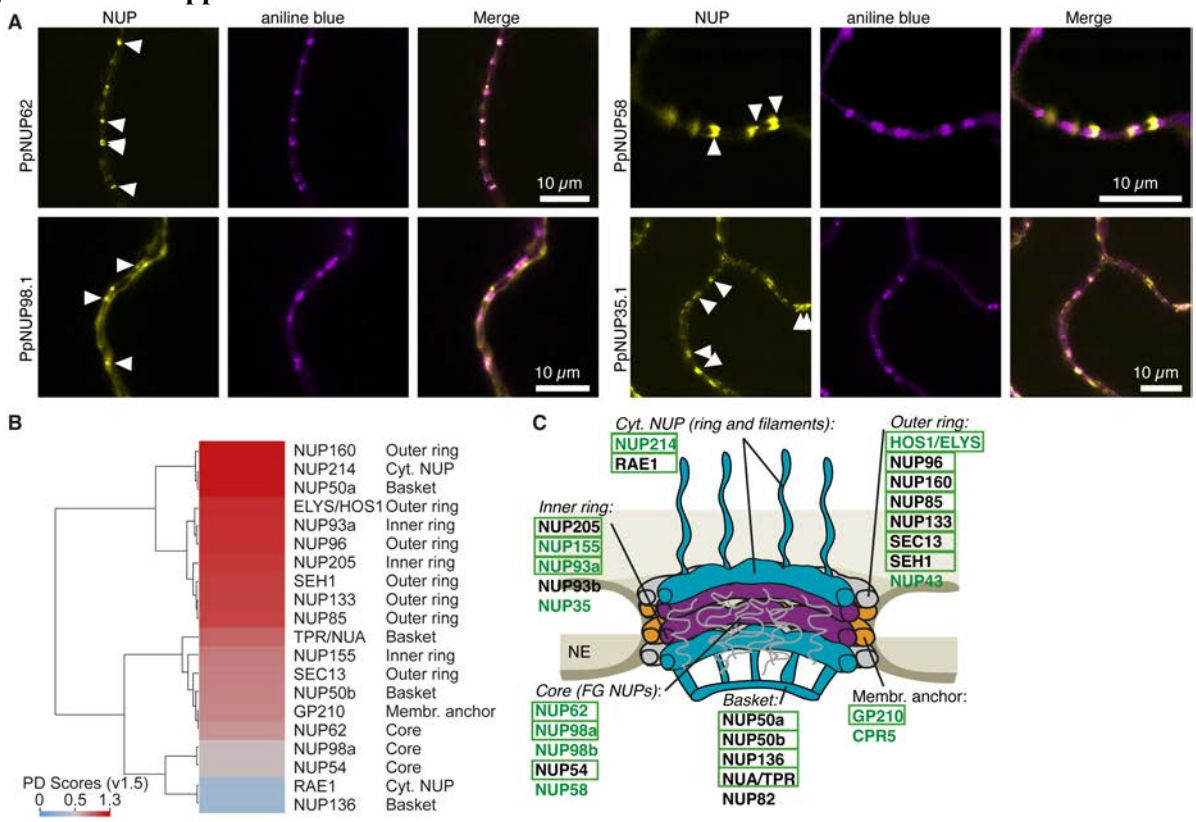

Figure 1. Identification of NUPs at PD. (**A**) Localization of NUPs from *Physcomitrium patens* at PD. **(B)** Hierarchical clustering of PD scores of Arabidopsis NPC components found in PD proteome preparations from 5-week-old Arabidopsis shoot tissues. Clustering based on Euclidean distance of PD scores (v1.5), which were averages of at least three replicate scores from separate tissue preparations. Color scale represents PD score values. PD scores above the high-confidence threshold of 0.5 are indicated in shades of red. (**C**) Scheme of an NPC embedded in the nuclear envelope with all NUPs studied in this work. NUPs listed in B are green boxed. Green letters: NUPs significantly enriched at PD in transient localization assays (Figure 2B, 3B). Green boxed black letters: NUP was identified in the proteome, but was not enriched at PD in transient localization assays. Corresponding AGI locus identifiers in table S2. Cytoplasmic NUP is abbreviated as Cyt. NUP, and membrane anchor as Membr. anchor.

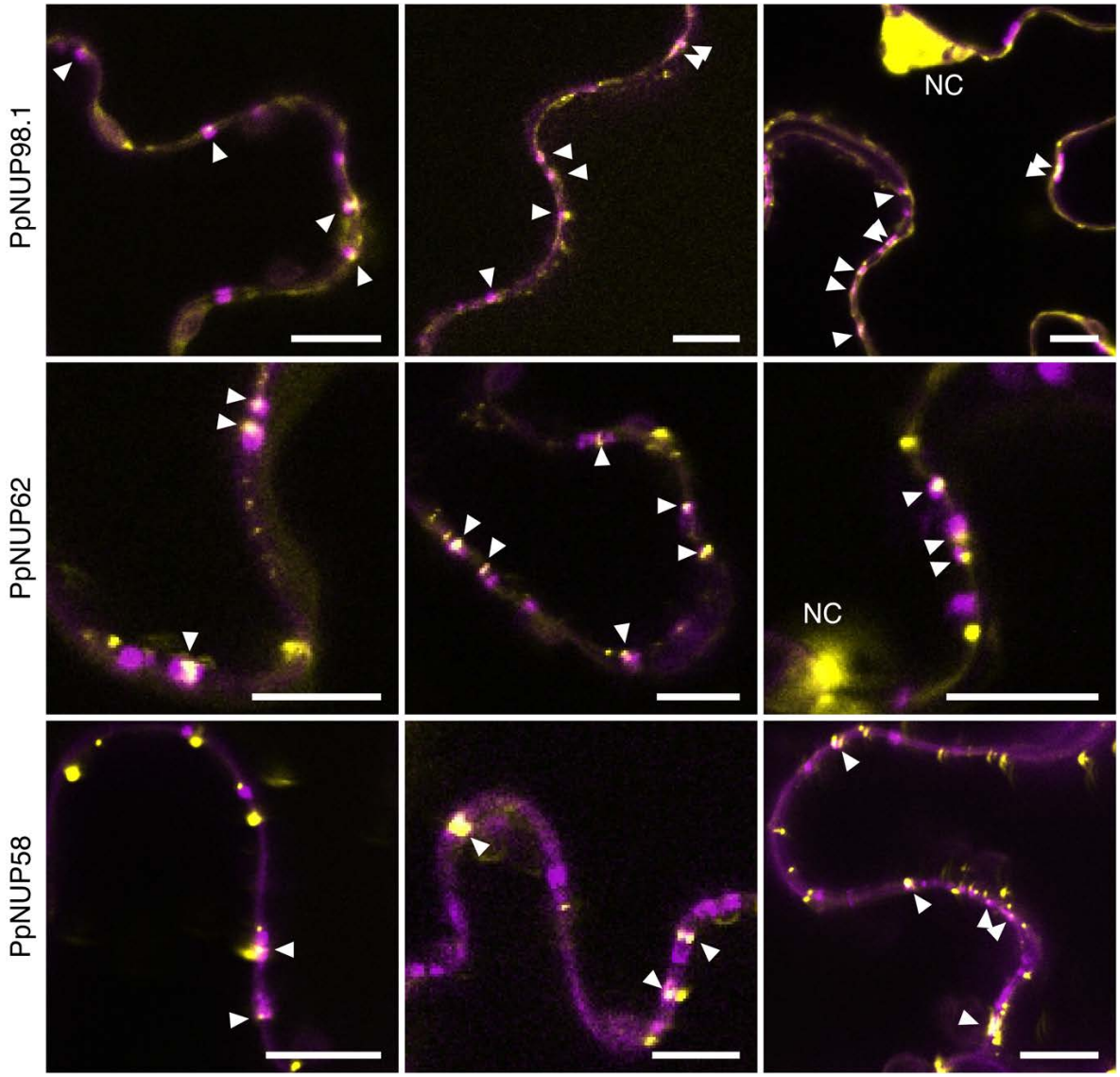

Figure 1-figure supplement 1. Overlay of *Physcomitrium patens* FG-NUPs with the PD marker aniline blue. Localization of FG-NUPs from *P. patens* in *N. benthamiana* epidermal cells visualized by confocal microscopy. FG-NUPs were fused at their C-terminus to mVenus (yellow) and expressed transiently under the control of the inducible XVE promotor. Aniline blue (purple) was infiltrated to stain callose, which accumulates in pit fields. Arrowheads indicate overlay between NUPs and aniline blue. For each NUP, a similar localization pattern appeared in at least three independent experiments. NC = nucleus. Scale bar: 10 µm.

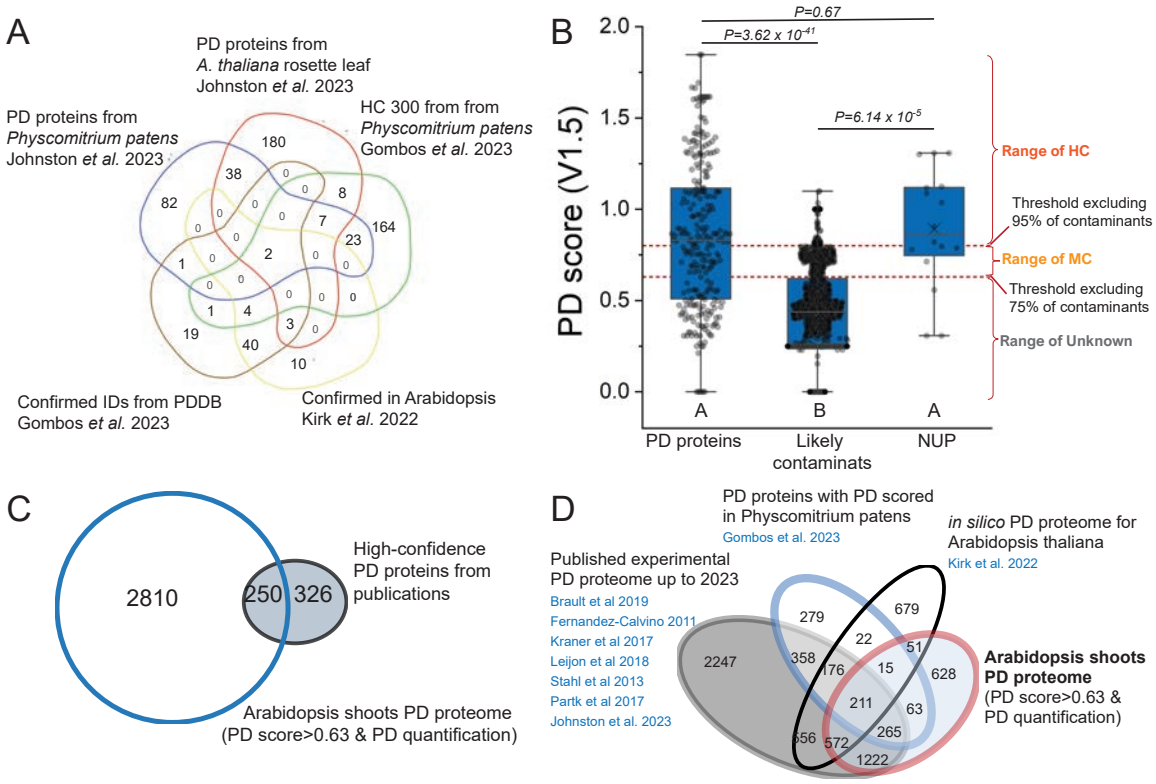

Figure 1-figure supplement 2. Arabidopsis shoot proteome and the comparison to other PD proteomes. (**A**), Venn diagram defining high-confidence PD proteins from previous publications, e.g., confirmed Arabidopsis PD proteins, and high confidence PD proteins identified in *Physcomitrium*, and in both *Physcomitrium* and Arabidopsis leaves (Gombos et al., 2023; Johnston et al., 2023; Kirk et al., 2022). These proteins were then used as high-confidence data set to establish the PD probability threshold and were labelled as 'PD proteins' in file S3. 43% of these proteins were quantified in our Arabidopsis shoot PD proteome. (**B**), PD Scores of nuclear pore components. PD Scores (v 1.5) are shown as box plots for high-confidence PD proteins (PD proteins), typical co-purifying proteins from plastid and mitochondria identified in Arabidopsis PD preparations (likely contaminants) and proteins of the nuclear pore complex (NUP). Dotted lines indicate two thresholds based on the frequency distribution for contaminant proteins and PD proteins. The median is shown as a gray line, the mean value is denoted by a + symbol, and the whiskers cover the 95thpercentile. PD Scores above 0.83 (the upper dotted line) indicate high-confidence (HC) PD proteins; scores between 0.63 and 0.83 (between the two dotted lines) signify medium-confidence (MC) PD proteins; and scores below 0.63 are considered low confidence (LC) as their PD Scores overlapped with 75% of the contaminants. These confidence clusters were annotated in file S3. The final Arabidopsis shoot PD proteome consists of proteins with PD scores above 0.63, which are also quantifiable in the PD fraction. Capital letters represent group statistical comparisons determined by Oneway-ANOVA. The p-values of pairwise comparison using Student's t-test, are indicated on the top of the boxes. (**C**), Overlap between the Arabidopsis shoot PD proteome and other PD proteomes. Proteins with a PD score >0.63 and quantifiable in PD fraction (Arabidopsis shoot PD proteome) were compared with nine representative PD proteome studies. In the current Arabidopsis shoot PD proteome, 80% of the proteins were previously identified in published PD proteomes. Combining PD enrichment and data analysis thresholding allowed us to determine the confidence levels of PD proteins and obtain a "cleaner" PD proteome. In total, we identified 5145 proteins from PD, CW, and TC fractions, with 3347 proteins having a PD score >0.63. Among them, 3062 proteins are quantifiable in the PD fraction, constituting our Arabidopsis shoot PD proteome. Among these, 2268 proteins are categorized as high-confidence PD proteins, while 792 proteins fall into the medium-confidence category (file S3). Additionally, we discovered 20 nuclear pore proteins (NUPs), with 15 of them surpassing the threshold and being included in the final PD proteome. Among these, 11 are classified as high-confidence PD proteins, while 4 are medium-confidence PD proteins (file S3, Figure 1-figure supplement 2B). (**D**)

Comparison of Arabidopsis shoot PD proteomes with various published PD proteomes. 80% of the proteins had been identified in previous studies.

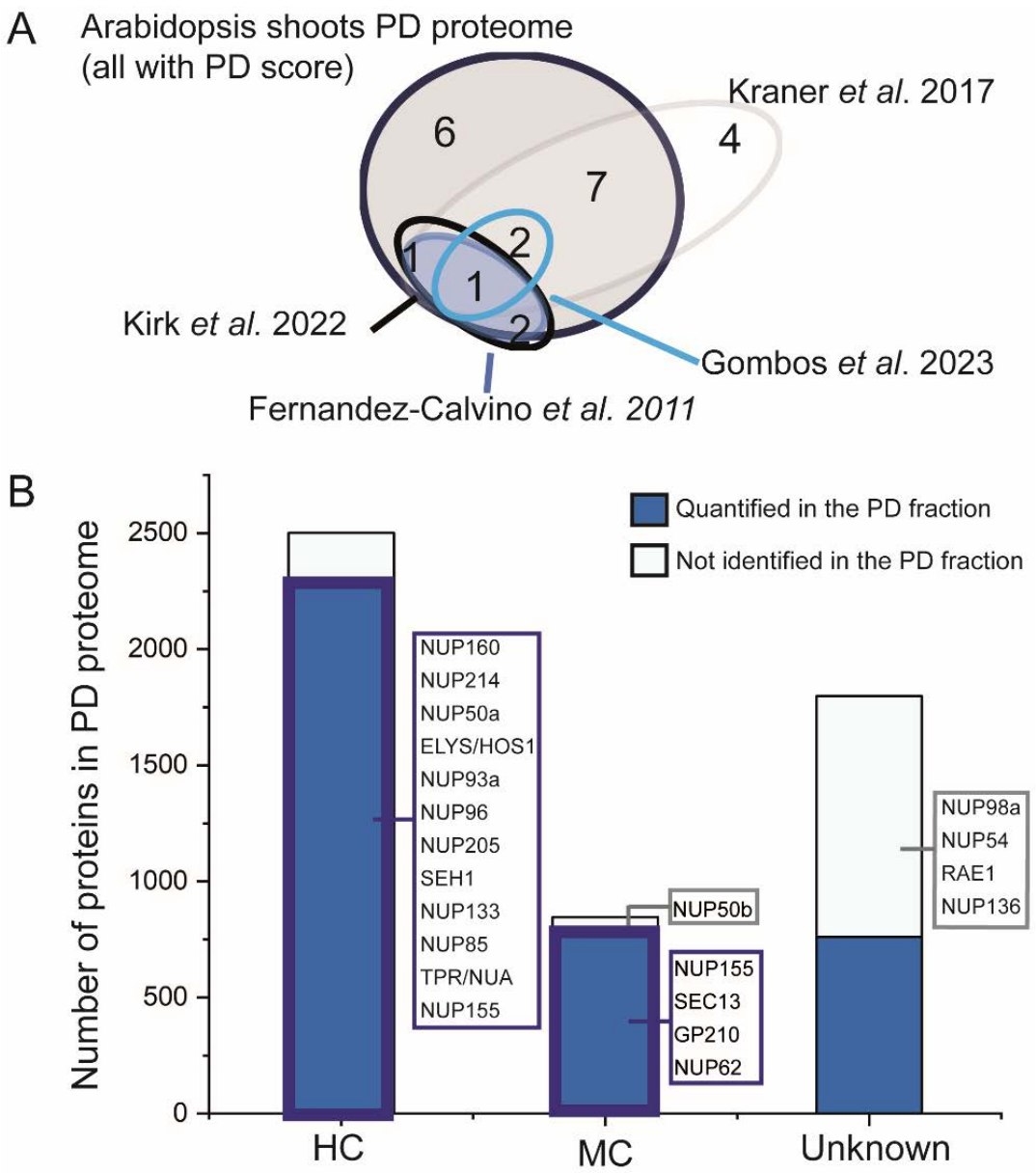

Figure 1-figure supplement 3. NUPs are found in Arabidopsis shoot proteome and other PD proteomes. (A), Comparison of NUPs in Arabidopsis shoot PD proteomes with published PD proteomes. Among the NUPs identified in the Arabidopsis shoot PD proteome, 73.3% (11 out of 15) were also detected in previously published PD proteomes. (**B**), Overview of identified proteins in the PD proteome. HC (PD score > 0.83), MC (0.83 > PD score > 0.63), and Unknown (PD score < 0.63). Purple-edged boxes in HC and MC mark proteins that meet Arabidopsis shoot PD proteome criteria (PD score > 0.63, quantifiable in PD fraction). Blue-edged boxes denote 16 NUPs within the Arabidopsis shoot PD proteome; Gray-edged boxes represent NUPs found also in other proteomes.

Figure 2 with 1 supplement

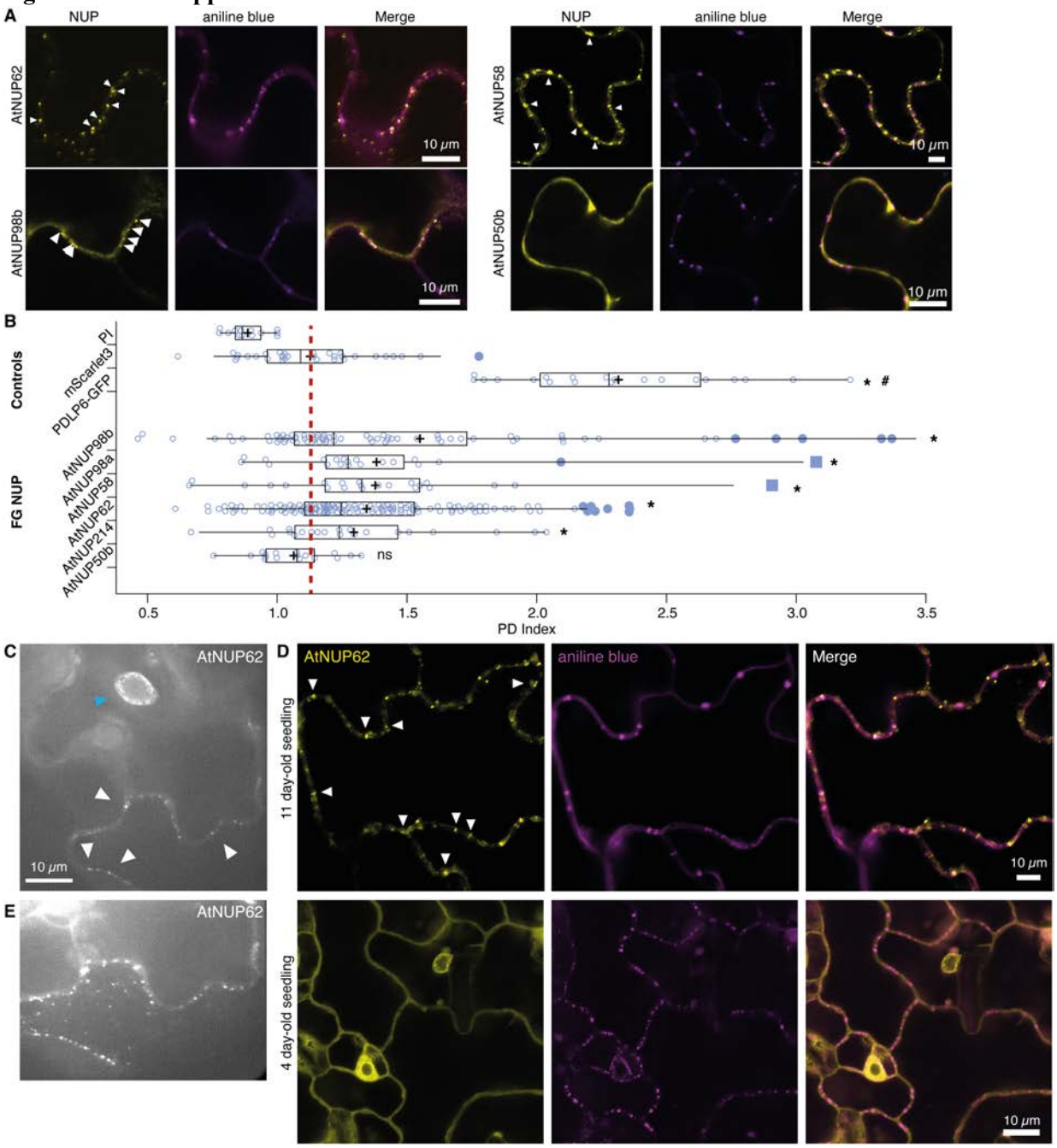

Figure 2. Dual localization of Arabidopsis FG NUPs. (A) Localization of selected Arabidopsis FG-NUPs after transient expression under the control of the β-estradiol-inducible XVE promotor in *N. benthamiana* epidermal cells using confocal microscopy. mVenus was fused to the C-terminus of different NUPs, except for NUP98a for which GFP was fused both N- and C-terminally (GFP-NUP98a-GFP). Aniline blue was infiltrated to detect callose in pit fields as a PD marker. Localization was repeated in three independent experiments with similar results. (**B**) Quantification of the PD localization by PD index. Red dashed line indicates the mean PD index of mScarlet3 (cytoplasmic control). PI, propidium iodide ('membrane impermeant dye'). Significantly ($p < 0.05$) increased PD indices compared to the cell wall or cytoplasmic controls are indicated by * and #, respectively. Kruskal-Wallis Test $p < 0.001$, p-values of Bonferroni corrected pairwise test are summarized in table S2. Median is represented by vertical line inside the box, mean is represented by the bold +. Values between quartiles 1 and 3 are represented by box ranges, and 5th and 95th percentile are represented by error bars. At least 15 images from 3 biological replicates were analyzed for each NUP. Independent localization data are shown in Figure 1-figure supplement 3. (**C-E**) Arabidopsis NUP62-GFP plants expressing NUP62 fused to GFP under its own

promoter. (**C**) The localization of NUP62-GFP in 11-day-old cotyledon epidermal cells was visualized by confocal microscopy (CSU10; 100x oil-immersion objective). Arrowhead: blue nucleus, white peripheral NUP62-GFP. **(D)** Localization of NUP62-GFP in cotyledonar epidermal cells of stably transformed 11-day-old (*top*) and 4-day-old (*bottom*) Arabidopsis lines. Cotyledons were immersed in aniline blue to detect callose in pit fields as PD markers. White arrowheads in D indicate overlay of NUPs and aniline blue. Scale bar: 10 µm. **(E)** Maximum intensity projection of 20 optical cross-sections taken at 1µm intervals of epidermal cotyledon cells expressing NUP62 fused to GFP under its own promoter (11-day-old seedling). Punctate localization of NUP62-GFP can also be found at the epidermis cell surface on the adaxial side of the cell.

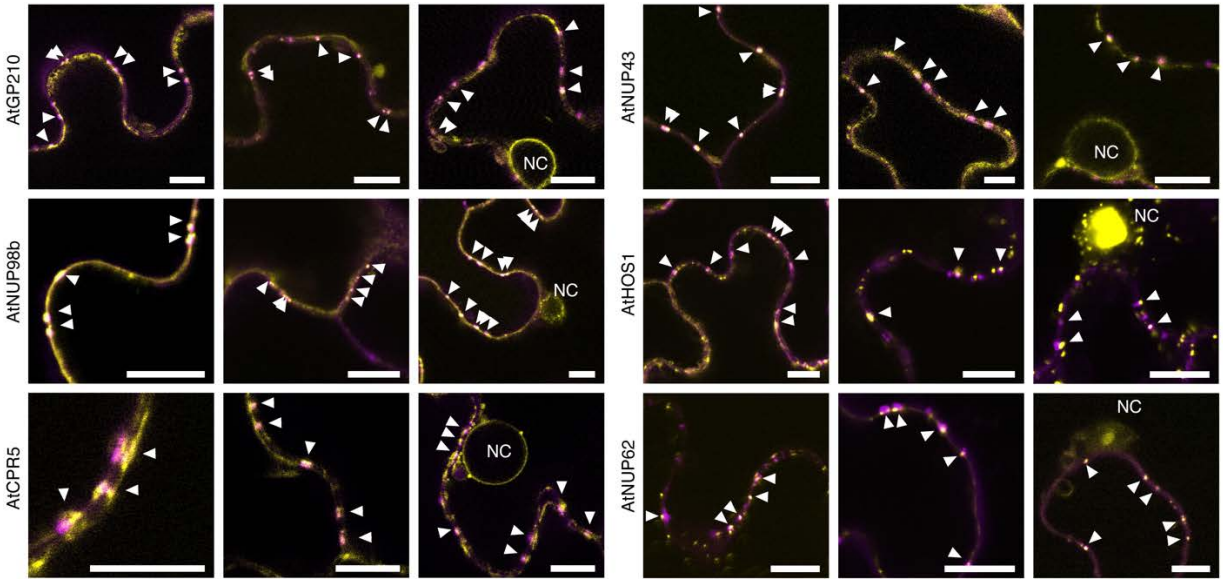

Figure 2-figure supplement 1. Arabidopsis NUP-FP localization overlays with a PD marker. Localization of Arabidopsis NUPs in *N. benthamiana* epidermal cells visualized by confocal microscopy. NUPs were fused at their C-terminus to mVenus or mCitrine (yellow) and expressed transiently under the control of the inducible XVE promotor. Aniline blue (purple) was infiltrated to stain callose that accumulates in pit fields. Arrowheads indicate overlay between NUPs and aniline blue. NUPs shown here were found to have a significant increased PD index values compared to negative controls in Figure 2. For each NUP, the localization pattern was reproducible in at least in three independent experiments. NC, nuclei. Note that for comparison, we here show the same images for NUP98B and NUP62 from Figure 2A again. Scale bar: 10 µm.

Figure 3

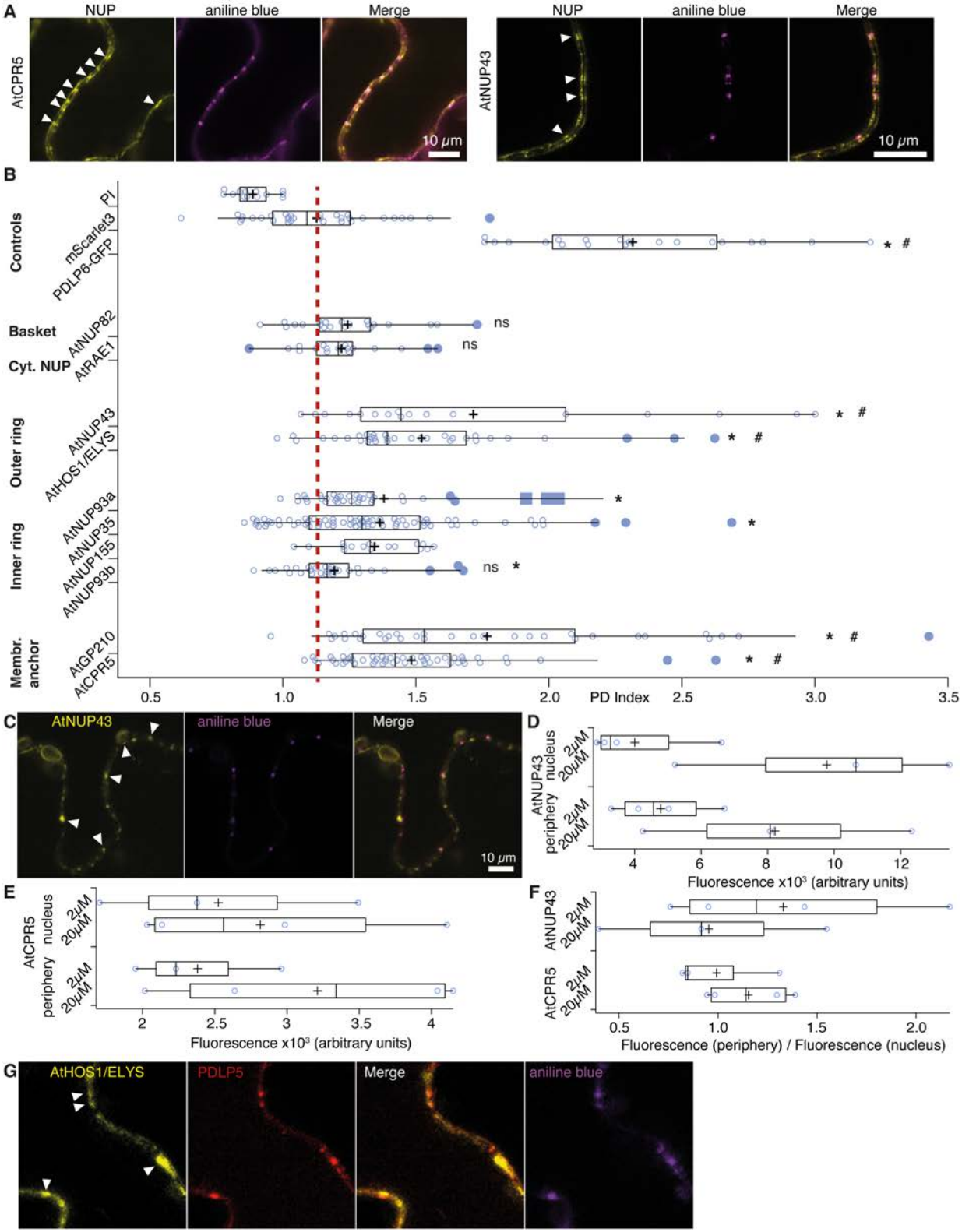

Figure 3. Dual localization of Arabidopsis scaffold and transmembrane NUPs. (A) Localization of Arabidopsis transmembrane (CPR5) and scaffold (NUP43) NUPs after transient expression under the control of the β-estradiol-inducible XVE promotor in *N. benthamiana* epidermal cells using confocal microscopy. mVenus was fused to the C-terminus of different NUPs. Aniline blue was infiltrated to detect callose in pit fields as PD marker. White arrowheads indicate overlay with aniline blue. Localization was repeated in three independent experiments with similar results. (**B**) Quantification of the PD localization

by PD index. Red dashed line indicates the mean PD index of mScarlet3 (cytoplasmic control). PI, propidium iodide ('membrane impermeant dye'). Significantly ($p < 0.05$) increased PD indices compared to cell wall or cytoplasmic controls indicated by * and #, respectively. Kruskal-Wallis Test $p < 0.001$, *p*-values of Bonferroni corrected pairwise test are summarized in table S2. Median: vertical line inside box, mean: +. Values between quartiles 1 and 3: box ranges, and 5th and 95th percentile are represented by error bars. At least 15 images from 3 biological replicates were analyzed for each NUP. Independent data in Figure 1-figure supplement 3. Control identical to Figure 2B. **(C**) NUP43-mCitrine localization at PD at 1/10 β-estradiol concentration and shortened induction time (not exceeding 10h). White arrowheads: overlay with aniline blue. **(D and E)** Quantification of the fluorescence intensity of NUP43-mCitrine (D) and CPR5-FP fusions (mVenus and mCitrine) (E) in the periphery and the nucleus after induction by 20µM or 2µM β-estradiol. **(F)** Periphery/nucleus fluorescence ratios in plants expressing NUP43-mCitrine or CPR5-FP fusions after expression is induced by 2 or 20µM β-estradiol. Box plots in (D-F) are based on a smaller subset of confocal images that show nucleus and peripheral fluorescence in one image; for individual conditions: $n \geq 3$ images from at least 2 independent repeats. Student´s t-test in (F) 2µM vs. 20µM estradiol: for NUP43, $p = 0.26$ and for CPR5, $p = 0.45$. (**G**) Localization of HOS1/ELYS-mCitrine and PDLP5-mScarlet3 co-expressed transiently under the control of the inducible XVE promoter in *N. benthamiana* epidermal cells. Aniline blue was infiltrated to stain callose that accumulates in pit fields. White arrowheads: overlay of HOS1/ELYS-mCitrine and PDLP5-mScarlet3 channels. Localization repeated in three independent experiments with comparable results.

Figure 4 with 4 supplements

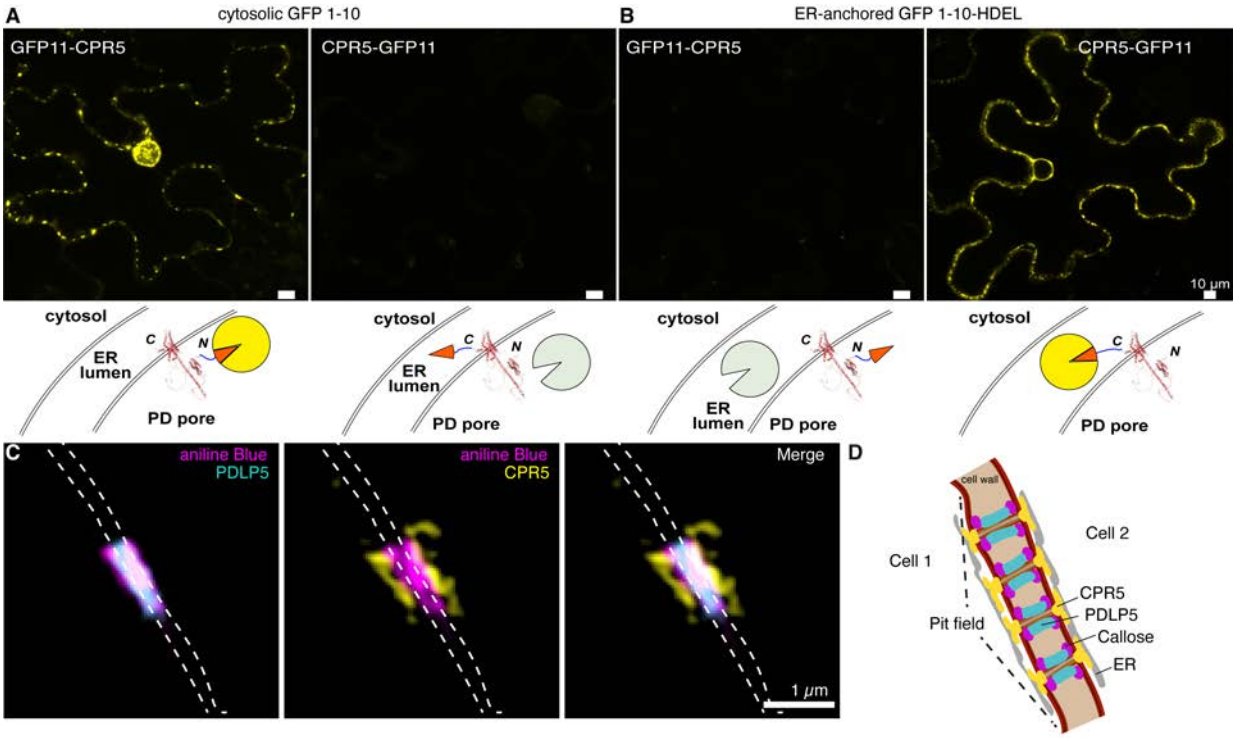

Figure 4. CPR5 topology and localization of CPR5 near PD orifices. Split-GFP membrane topology to test for the orientation of CPR5 in the nuclear pore membrane and the ER at PD. (**A**) *(left)* Fluorescence reconstitution at PD between a cytosolic non-fluorescent GFP domain lacking β-sheet 11 (GFP1-10; the circle missing a wedge) and a fusion of the GFP11 to the N-terminus of CPR5 (the red wedge). Since reconstitution occurs at PD, each cartoon indicates reconstitution in the intermembrane space between ER/desmotubule and plasma membrane. *(right)* Cytosolic GFP1-10 and GFP11fusion to C-terminus of CPR5. (**B**) *(left)* ER-retained GFP1-10-HDEL and GFP11 fused to N-terminus of CPR5. *(right)* ER-retained GFP1-10-HDEL and fusion of GFP11 to C-terminus of CPR5. Repeated independently 3 times with comparable results. (**C**) CPR5-mCitrine close to the orifices of PD by Structured Illumination Microscopy in *N. benthamiana* leaves co-infiltrated with XVE:PDLP5-mScarlet3 and XVE:CPR5-mCitrine. Prior to imaging, leaves were infiltrated with aniline blue. PDLP5-mScarlet3: turquoise, CPR5-mCitrine: yellow, aniline blue: magenta. Repeated independently four times with comparable results. **(D)** Cartoon approximately to scale, illustrating PD in pit field between adjacent cells with callose marked mangenta, PDLP5 turquoise, CPR5 yellow.

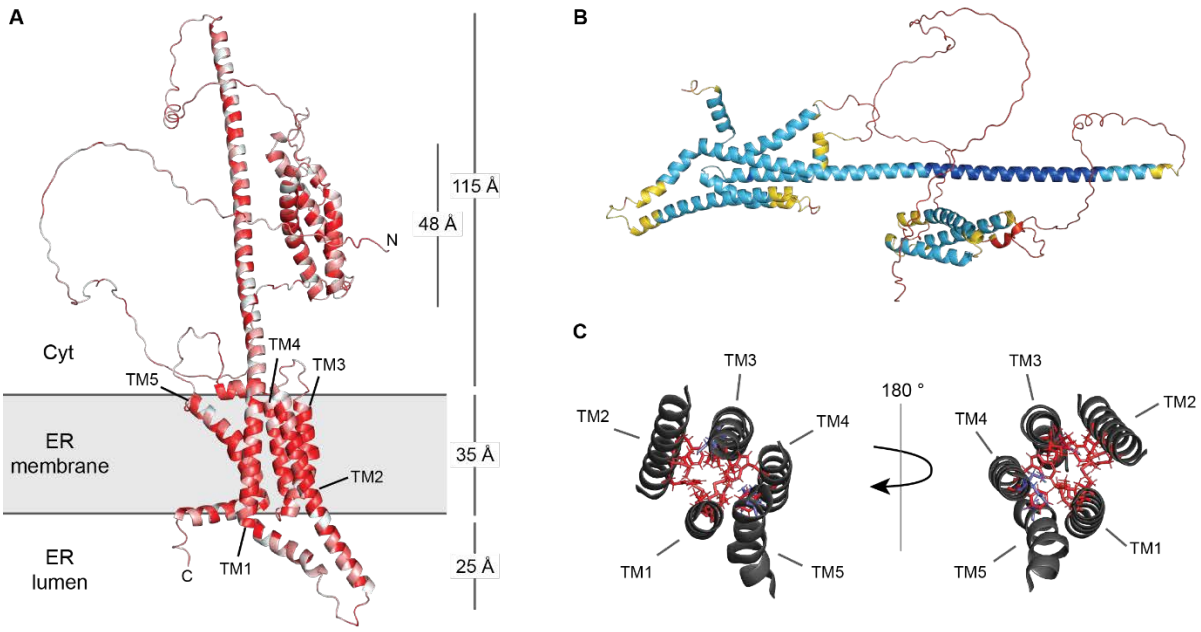

Figure 4-figure supplement 1. Predicted structure of monomeric CPR5 and model for integration into ER-derived membranes. Topological studies using the split-GFP system (Figure 4A,B, Figure 4-figure supplement 3) are consistent with a localization of the CPR5 C-terminus in the ER lumen, while its N-terminus extends into the cytoplasm. (**A**), CPR5 is composed of a N-terminal, disordered region (residues 1-106), a soluble domain formed by 3 α-helices (107-192), linked by a second disordered region (193- 265) to an approx. 115 Å long, central α-helix (266-342). Hydrophobic residues (red) of the central helix (TM1) and 4 shorter helices (TM2-TM5) form a transmembrane domain spanning approx. 35 Å, consistent with the expected thickness for ER-derived membranes. C-terminus and helical extensions of TM1 and TM2 reach into the ER lumen. (**B**), Structure colored by per-residue prediction confidence (pLDDT; dark blue: 90-100, light blue: 50-70, yellow: 50-70, red: < 50). Low confidence values (red) may indicate regions that are either intrinsically disordered or assume a structure when interacting with other proteins and therefore could partake in formation of complexes with NUPs. (**C**), View of transmembrane helical bundle from ER lumen (left) and cytoplasm (right). Amino acid side chains spanning between transmembrane helices are colored by hydrophobicity (blue: hydrophilic, red: hydrophobic). The CPR5 transmembrane domain is not predicted to form a solvent-accessible pore.

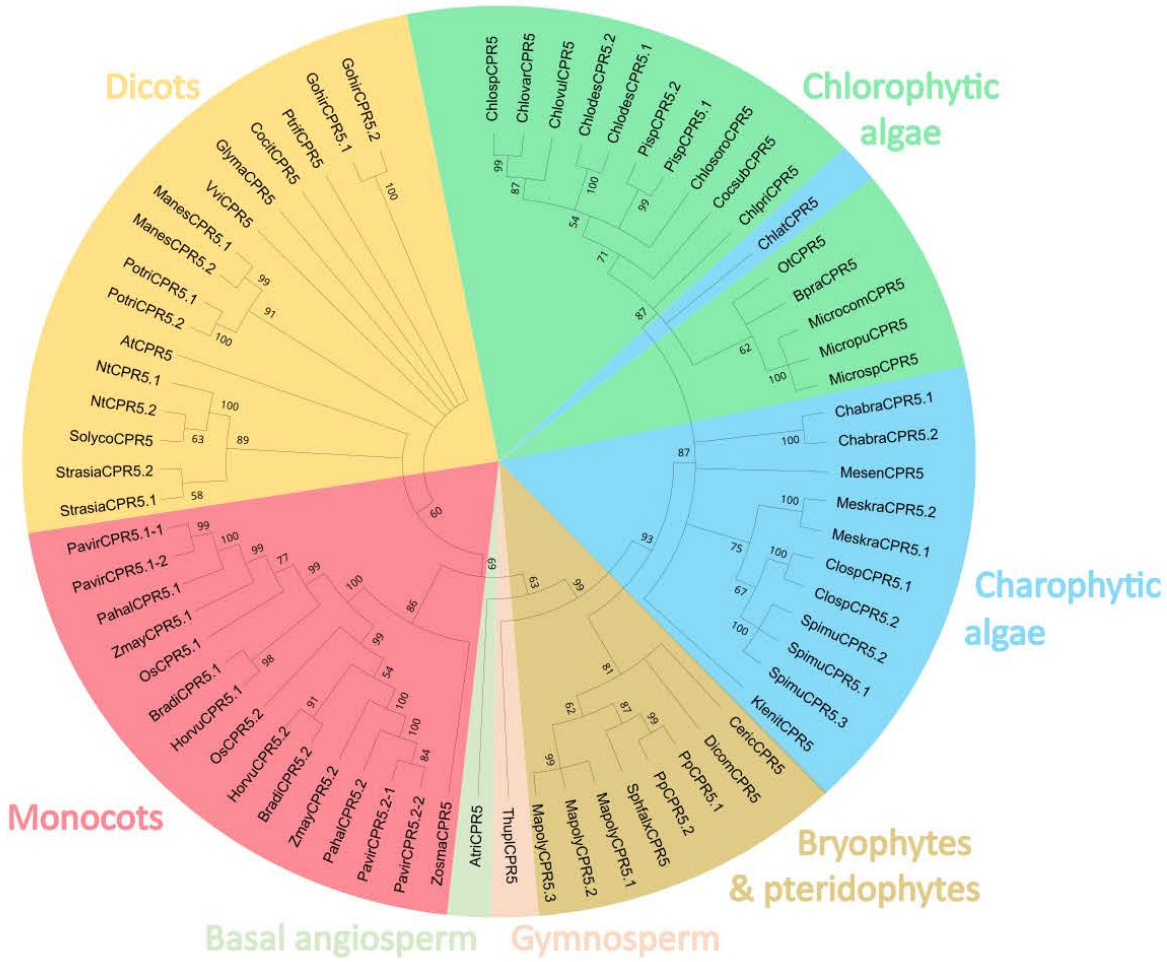

Figure 4-figure supplement 2: Phylogenetic analysis of CPR5 sequences. The accession numbers and the abbreviations corresponding to the mature protein sequences used for this analysis are given in table S7. The analysis was performed as described in the "Materials and Methods" section.

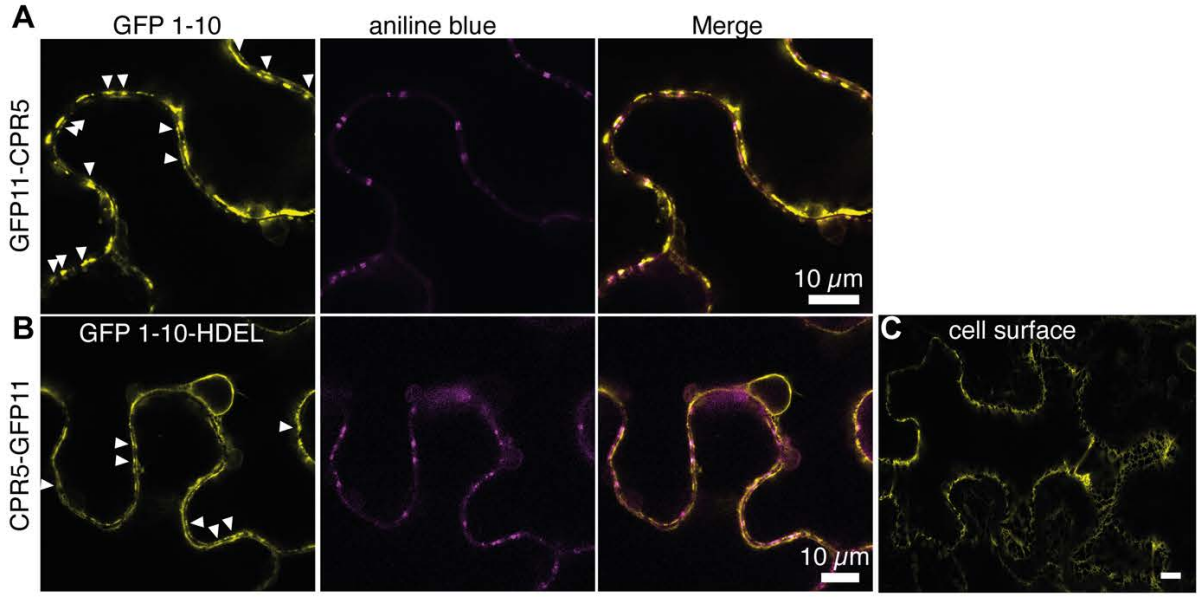

Figure 4-figure supplement 3. The C-terminus of CPR5 faces ER lumen. (A), Transient co-expression of GFP11-CPR5 and cytosolic GFP1-10 in *N. benthamiana* leaves, same cell as shown in Figure 4. *Left*, GFP channel. Reconstitution can be observed also at PD (arrowheads). *Middle*, aniline blue. *Right,* merge. (**B**), *N. benthamiana* epidermal cells transiently expressing CPR5-GFP11 and ER luminal GFP1-10-HDEL, same cell as shown in Figure 4. *Left*, GFP channel. Reconstitution can be observed also at PD (arrowheads); *middle*, aniline blue*; right,* merge. (**C**), Surface view of the same cell as in B, showing reconstitution in the ER.

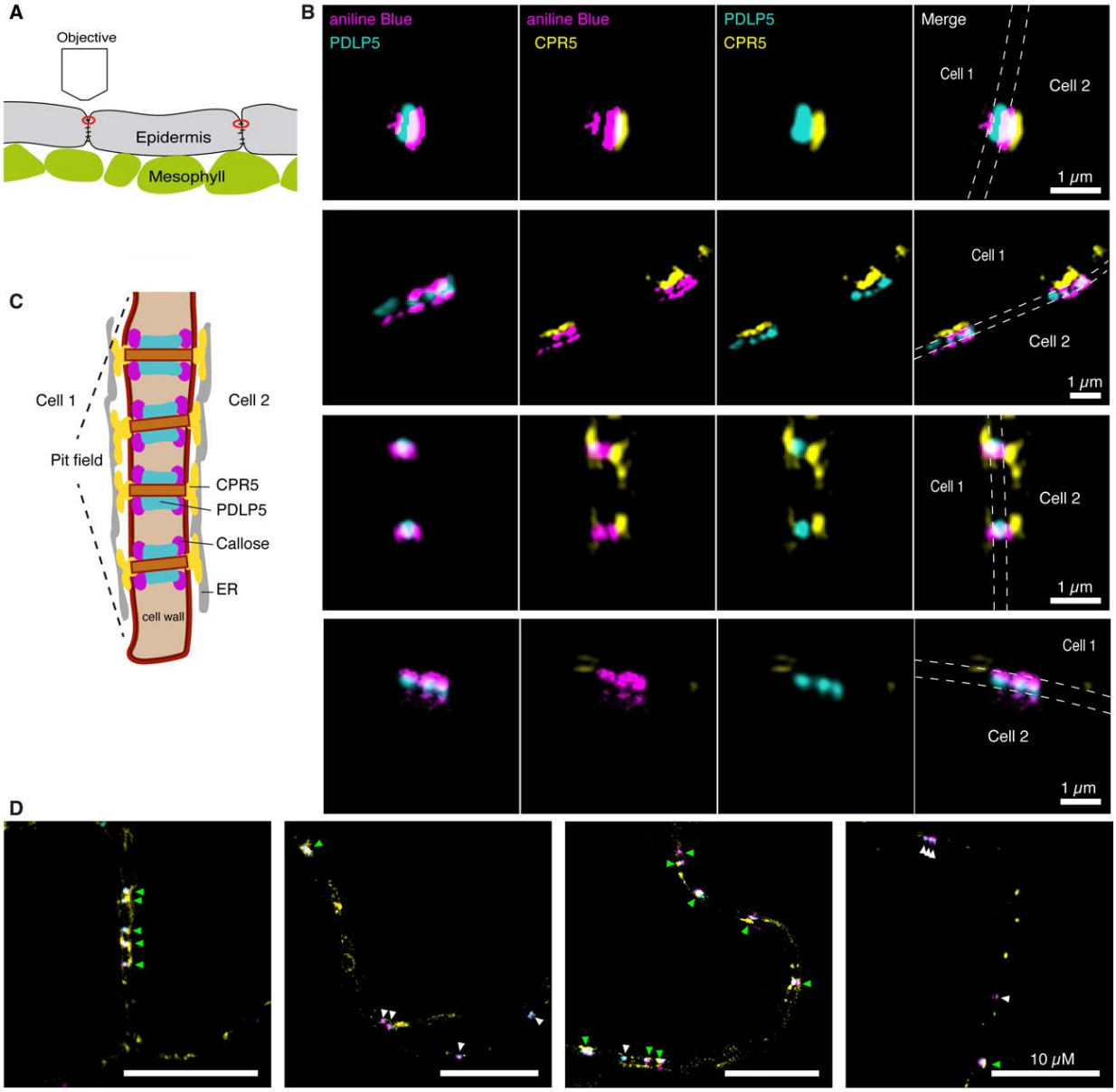

Figure 4-figure supplement 4. **CPR5-mCitrine localizes at the orifices of PD**. (**A),** Cartoon showing analyzed PD: only PD most proximal to the cover glass and objective were analyzed to reduce effects caused by scattering of light due to cell wall. (**B),** SIM in *N. benthamiana* leaves co-infiltrated with XVE:PDLP5-mScarlet3 and XVE:CPR5-mCitrine. Prior to the imaging, leaves were infiltrated with aniline blue. PDLP5-mScarlet3 in turquoise, CPR5-mCitrine in yellow, and aniline blue in magenta.

Comparable results were obtained in four independent experiments. Dashed lines indicate approximation of cell wall boundaries. (**C),** Cartoon of pit field and localization of PDLP5 and CPR5. Fluorescence reporting on CPR5 in (B) extends laterally 200-1000 nm in the epidermal cell wall. Previously, the lateral extension of individual PD pores in the cell wall was estimated to 100 nm for basal trichome cell walls and 187 nm for epidermal cell walls (Faulkner et al., 2008; Fitzgibbon et al., 2010). The resolution achieved with SIM was not high enough to resolve single PD or determine whether pit fields consist of several simple PD (as shown in C) or a few complex (H-shaped/twinned) PD. (**D**), SIM in *N. benthamiana* leaves co-infiltrated with XVE:PDLP5-mScarlet3 and XVE:CPR5-mCitrine. Green arrowheads indicate overlay between CPR5-mCitrine, PDLP5-mScarlet3 and aniline blue; white arrowheads indicate overlay between PDLP5-mScarlet3 and aniline blue, without CPR5-mCitrine. PDLP5-mScarlet3 in turquoise, CPR5-mCitrine in yellow, and aniline blue in magenta.

Figure 5 with 1 supplement

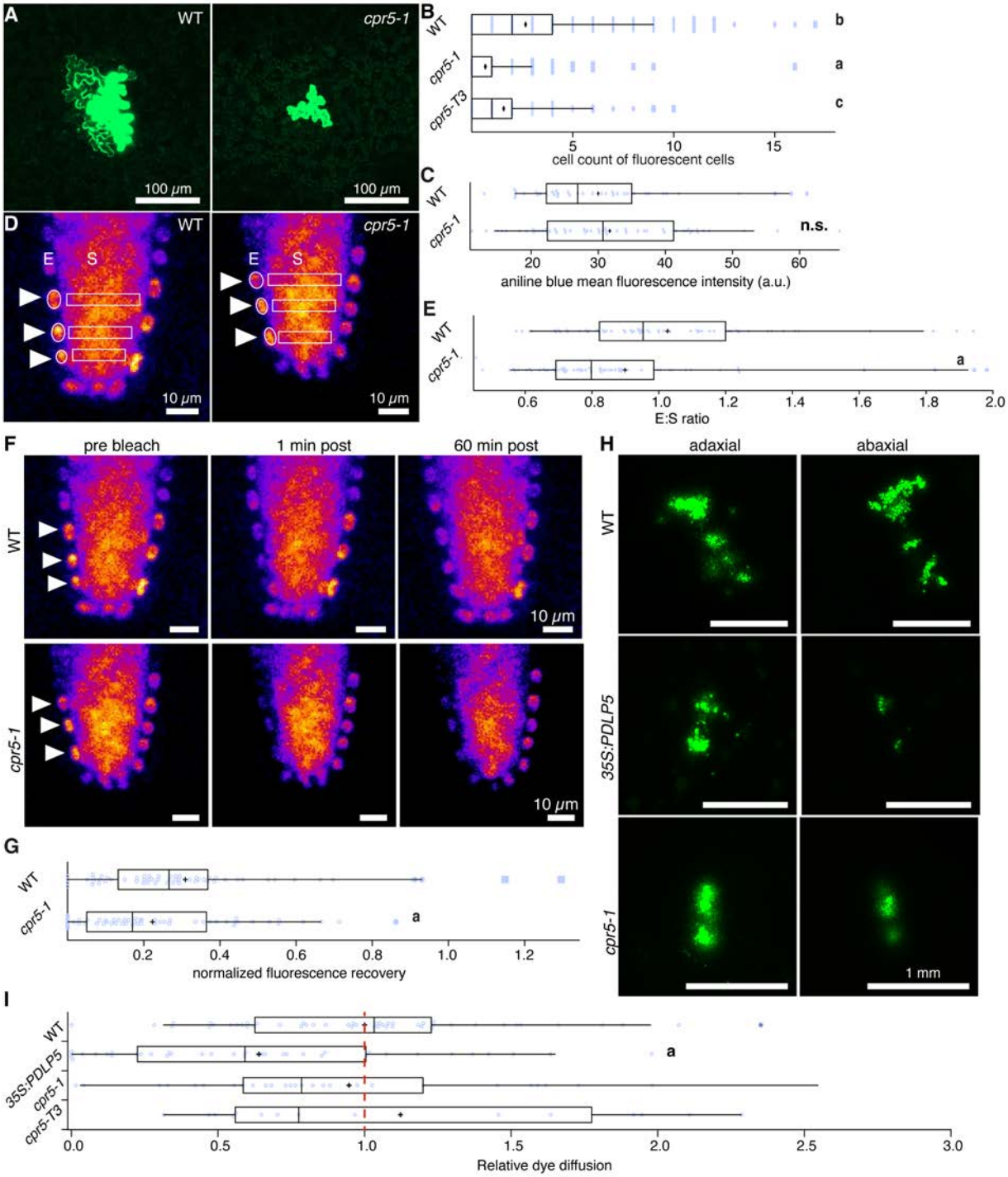

Figure 5. Defects in cell-to-cell transport of kDa-sized cargo in *cpr5* mutants. (A) Example images of intercellular 2xmEGFP movement in wild type (WT, *left*) and *cpr5-1* (*right*) Arabidopsis leaves. Leaves were bombarded with gold particles coated with p35S:mEGFP-mEGFP DNA plasmids 24 h prior to the analysis by confocal microscopy (fusion protein abbreviated as 2xmEGFP). **(B)** Quantification of the intercellular spread of mEGFP by counting fluorescent cells in the GFP channel. $n_{(WT)} = 594$ bombarded cells, 17 independent biological replicates: $n_{(cpr5\text{-}1)} = 278$ bombarded cells, 6 independent biological replicates. $n_{(cpr5\text{-}T3)} = 99$ bombarded cells, four independent biological replicates. **a** indicates significant difference to WT with $p_{(cpr5\text{-}T3)} = 0.0004$; **b** indicates significant difference to WT with $p_{(cpr5\text{-}1)} < 10^{-15}$; $p_{(cpr5\text{-}1 \text{ vs. } cpr5\text{-}T3)} = 0.0002$ (Kruskal-Wallis test with Bonferroni correction for pairwise comparison). **(C)**

Callose quantification. $n_{(WT)}$ = 4 independent experiments, $n_{(cpr5\text{-}1)}$ = 5 independent experiments, graph summarizes all experiments. Student´s *t*-test p = 0.48. **(D)** Sum projections showing SHR–GFP distribution in WT (*left*) and *cpr5-1* mutant (*right*) root. White circles and boxes indicate positions of endodermis nuclei (E, arrows) and corresponding regions in the stele (S, white boxes). **(E)** Quantification of SHR–GFP endodermis:stele ratio (E:S) for WT and *cpr5-1* mutant. $n_{(WT)}$ = 62 nuclei, $n_{(cpr5\text{-}1)}$ = 62 nuclei, with 3-4 nuclei analyzed per root. **a** indicates significantly decreased E:S in *cpr5-1* mutant, based on Mann-Whitney U test with p = 0.0006. **(F)**, Sum projections showing SHR–GFP distribution in WT (*top*) and *cpr5-1* (*bottom*) background. **(G)**, Quantification of relative SHR–GFP fluorescence recovery for WT and *cpr5-1* mutant after 1 h. Fluorescence recovery was normalized to a control nucleus in the endodermis (see Methods and Figure 5-figure supplement 1F). n(WT) = 59 bleached nuclei, n(*cpr5-1*) = 59, per root 3-4 nuclei were bleached. Student´s t-test p = 0.037 indicating significantly decreased fluorescence recovery after 60 min. **(H and I)** PD permeabilities examined by CFDA/CFSE-based DANS dye loading assays. **(H)** Epifluorescence reporting on CF diffusion in the epidermis of the adaxial (*left*) and abaxial (*right*) side of the leaf. WT *(top), 35S:PDLP5* (*middle*), and *cpr5-1* (*bottom*). Bars, 1 mm. **(I)** Quantification of CF diffusion in WT and mutant lines. $n_{(WT)}$ = 49 plants, 7 independent biological replicates; $n_{(35S:PDLP5)}$ = 38 plants, 5 independent biological replicates; $n_{(cpr5\text{-}1)}$ = 29 plants, 5 independent biological replicates; $n_{(cpr5\text{-}T3)}$ = 15 plants, 5 independent biological replicates. Fluorescent areas on the abaxial side were identified using auto threshold and Fiji YEN-algorithm with user modifications. The same threshold setting was used for the adaxial side. The extent of dye diffusion was quantified by the ratio between the areal spread of fluorescence on the abaxial side and the areal spread of fluorescence on the adaxial side. **a** indicates significantly different at the α = 0.032 level according to Bonferroni-corrected pair wise comparison following Kruskal-Wallis analysis.

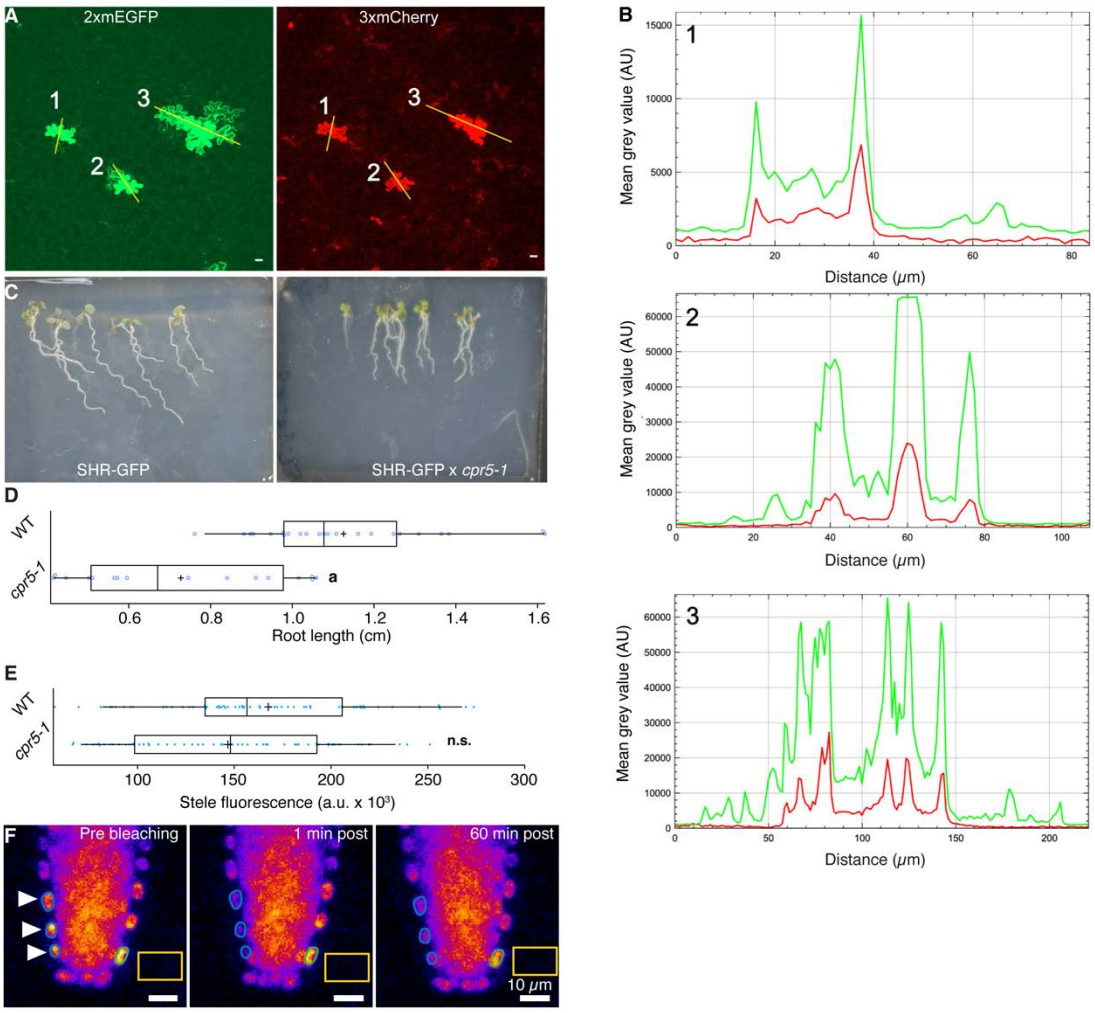

Figure 5-figure supplement 1. Intercellular transport assays in *cpr5-1* mutants. (A), Example of three different clusters (1, 2, and 3) of fluorescent cells after bombardment in a WT Arabidopsis leaf. Each cluster reports a successful bombardment event. Left, GFP channel, right, mCherry channel. 24 h prior to the experiment, leaves were co-bombarded with gold particles coated with p35S:mEGFP-mEGFP (2xmEGFP). DNA plasmids and gold particles coated with p35S:mCherry-mCherry-mCherry (3xmCherry). (**B),** Profile plots across the different clusters, 1, 2, and 3 as shown in A. Yellow lines in A indicate the position for the profile. The bombarded cell marked with 3xmCherry overlays with the brightest cell in the GFP channel. (**C),** Six-day old seedlings with *shr*/pSHR:SHR-GFP in WT Col-0 background *(left)* and *shr*/pSHR:SHR-GFP in the *cpr5-1* background (*right*) grown on ½ MS agar. **(D),** Quantification of the root length of 6-day old WT and *cpr5-1* mutant background seedlings. $n_{(WT)} = 23$ roots, four independent experiments, $n_{(cpr5\text{-}1)} = 16$ roots, three independent experiments. **a** Significantly decreased root length in *cpr5-1* mutant, based on Student´s *t*-test with $p = 0.00002$. **(E),** Quantification of SHR-GFP stele baseline fluorescence in *cpr5-1* mutant and WT background. $n_{(WT)} = 62$ stele ROIs, $n_{(cpr5\text{-}1)} = 62$ stele ROIs, with 3-4 ROIs analyzed per root. **n.s.,** no significant difference in fluorescence intensity based on Mann-Whitney U test with $p = 0.074$. **(F)**, SHR–GFP fluorescence recovery after photobleaching (FRAP) in homozygous *shr*/pSHR:SHR-GFP root endodermal cells (arrow heads). Note that for comparison, we here show the same sum projections as in Figure 5F (*top*). Blue circles show the position of ROIs for FRAP. Green circle shows the position of ROI for control nucleus used for normalization (see Methods). Yellow square shows the position for mean background fluorescence used for correction (see Methods).

Tables

table S1. Genome-wide search for potential phase-separating proteins with FG repeats. The 15 genes with the highest number of FG motifs within a 200-amino acid window in the *Physcomitrium* genome. For the list summarizing the genome-wide search for FG containing genes, see file S1. For Arabidopsis NUPs see file S2.

Gene	max #FG in 200 aa window	Predicted function
Pp3c26_7720	28	NUP96
Pp3c3_17910	28	NUP 98.1
Pp3c3_28570	25	NUP 98.2
Pp3c26_7680	25	NUP 98.3
Pp3c8_3950	21	NUP 98.4
Pp3c15_14630	19	NUP62
Pp3c14_14130	17	NUP54.1
Pp3c17_4470	16	inter-alpha-trypsin inhibitor heavy chain-related
Pp3c24_6760	14	NUP58
Pp3c13_12950	14	NUP214
Pp3c10_15930	13	NUP54.2
Pp3c10_15937	13	NUP54.3
Pp3c7_12210	12	zinc finger (CCCH-type) family protein
Pp3c24_6760	11	NUP58
Pp3c13_24530	10	Epidermal growth factor receptor substrate 15-like 1

table S2. List of known Arabidopsis NUPs and summary of localization results. *p*-values calculated from Bonferroni-corrected pairwise comparison between the tested NUP with propidium iodide marked by *; *p*-values calculated from Bonferroni-corrected pairwise comparison between the tested NUP and free mScarlet3 marked by #. Index is short for PD index (see also Figure 2 and 3). NA: not assessed. FG-NUPs in red.

NUP	AGI	Localization at NPC	Tested for localization
NDC1	AT1G73240	membrane anchor	NA
Gp210	AT5G40480	membrane anchor	index = 1.77, *** = 2x10^{-9}; # = 3x10^{-6}**
CPR5	AT5G64930	membrane anchor	index = 1.48, *** = 7x10^{-8}; # = 0.0001**
PNET1	AT1G07970	membrane anchor	NA
NUP155	AT1G14850	inner ring	index = 1.34, *** = 0.002**; # = 1.0
NUP93a	AT2G41620	inner ring	index = 1.38, *** = 0.001**; # = 1.0
NUP35/MPPN	AT3G16310	inner ring	index = 1.36, *** = 0.0002**; # = 0.549
NUP93b	AT3G57350	inner ring	index = 1.19, * = 0.43; # = 1.0
NUP188	AT4G38760	inner ring	NA
NUP205	AT5G51200	inner ring	NA
NUP160	AT1G33410	outer ring	NA
Seh1	AT1G64350	outer ring	NA
NUP96	AT1G80680	outer ring	NA
NUP133	AT2G05120	outer ring	NA
Sec13	AT2G30050	outer ring	NA
Elys/HOS1	AT2G39810	outer ring	index = 1.52, *** = 3x10^{-7}; # = 0.001**
NUP107	AT3G14120	outer ring	NA
NUP43	AT4G30840	outer ring	index = 1.72, *** = 3x10^{-6}; # = 0.006**
NUP75/85/SBB1	AT4G32910	outer ring	NA
NUP98a	AT1G10390	core FG-NUP	index = 1.38, *** = 0.006**; # = 1.0
NUP54	AT1G24310	core FG-NUP	NA
NUP98b	AT1G59660	core FG-NUP	index = 1.55, *** = 0.0001;** # = 0.276
NUP62	AT2G45000	core FG-NUP	index = 1.34, *** = 0.0001;** # = 0.357
NUP58	AT4G37130	core FG-NUP	index = 1.37, *** = 0.001;** # = 1.0
CG1	AT1G75340	cytoplasmic FG-NUP	NA
GLE1	AT1G13120	cytoplasmic NUP	NA
NUP214	AT1G55540	cytoplasmic FG-NUP	index = 1.29, *** = 0.041;** # = 1.0
Rae1	AT1G80670	cytoplasmic NUP	index = 1.22, * = 0.301; # = 1.0
Aladin	AT3G56900	cytoplasmic NUP	NA
MOS7/NUP88	AT5G05680	cytoplasmic NUP	NA
NUP50a	AT1G52380	basket FG-NUP	NA
NUA/TPR/ATTPR	AT1G79280	basket	NA
NUP1/NUP136	AT3G10650	basket FG-NUP	NA
NUP50b	AT3G15970	basket FG-NUP	index = 1.06, * = 1.0; # = 1.0
NUP82	AT5G20200	basket	index = 1.24, * = 0.1; # = 1.0

table S4. NPC components identified in published cell wall/PD proteomes

NUP	Reference
CPR5	(Kraner et al., 2017)
NUP93a	(Kirk et al., 2022)
NUP155	(Bayer et al., 2006; Fernandez-Calvino et al., 2011; Kraner et al., 2017)
SEC13	(Bayer et al., 2006; Gombos et al., 2023; Kraner et al., 2017)
NUP205	(Kirk et al., 2022)
NUA	(Gombos et al., 2023)
NUP50a *	(Gombos et al., 2023; Kraner et al., 2017; Li et al., 2024)
GP210	(Kraner et al., 2017)
NUP35	(Kraner et al., 2017)
HOS1	(Kraner et al., 2017)
NUP43	(Kraner et al., 2017)
NUP62	(Kraner et al., 2017)
NUP214	(Kraner et al., 2017)
NUP82	(Kraner et al., 2017)
NDC1 *	(Li et al., 2024)

* identified by TURBO-ID using PD proteins

table S5. Nuclear localization and observation of puncta in the cell periphery, consistent with PD localization by other laboratories

NUP	Transient expression	Stable transformation/ promoter	Reference
CPR5	*p35S:YFP-CPR5*	*p35S:GFP-CPR5/cpr5-1*	(Gu et al., 2016)
CPR5*	*p35S:CFP-CPR5*		(Peng et al., 2022)
NUP98a	*p35S:GFP-Dra2-GFP*	*p35S:NtDra2-GFP*	(Gallemí et al., 2016)
NUP155	*p35S:Nup155-cYFP+p35S:nYFP-CPR5*		(Gu et al., 2016)
HOS1	*p35S:HOS1-GFP*		(Lee et al., 2012)
NUP62	*p35S:Nup62-nYFP+p35S:FLC-cYFP*		(Chen et al., 2023)

* split-FP analysis indicated interaction of CPR5 with PRL1 and FIP1

table S6. Membrane/microtubule anchor proteins in NPC and ciliary gates across kingdoms

Organism/ location	# TM	Yeast	Mammalian	Chlamydomonas	Arabidopsis	*P. patens*	Ref.
NPC lumenal ring	1	POM152	GP210	n.p.	GP210	*Pp3c27_1470V3.1*	(Collins et al., 2023; Tamura et al., 2010)
NPC	1	POM121	POM121	n.p.	n.p.	n.p.	
NPC	6	NDC1	NDC1	*Cre03.g197550.t1.2*	NDC1	*Pp3c23_16320V3.1*	(Collins et al., 2023; Mansfeld et al., 2006)
NPC	3	POM33	TMEM33	*Cre02.g099650.t1.2*	*At3g02420*	*Pp3c7_9290V3.1*	this work
Ciliary gate	3	NPHP	TMEM218	*CEP290*	n.p.	n.p.	(Blasius et al., 2019; Craige et al., 2010; Epting et al., 2022; Li et al., 2016; Tang et al., 2020)
NPC	2	POM34	TMEM209	n.p.	PNET1 (*At1g07970*)	*Pp3c12_22070V3.1*	[48]
NPC green lineage	5	n.p.	n.p.	n.p.	CPR5	*Pp3c21_530V3.1* *Pp3c22_5670V3.1*	(Arra et al., 2024; Gu et al., 2016)

n.p. not present based on database searches

table S7. Accession numbers of CPR5 homologs used for the phylogenetic analysis shown in figure S6.

Protein name	Accession number	Species	Phylogeny	
ChabraCPR5.1	GBG69762.1	*Chara braunii*	Charophyta	Charophyceae
ChabraCPR5.2	GBG89669.1	*Chara braunii*	Charophyta	Charophyceae
ChlatCPR5	jgi|Chlat1|5100|Chrsp33S05109	*Chlorokybus atmophyticus*	Charophyta	Chlorokybophy-ceae
ClospCPR5.1	GJP55885.1	*Closterium*	Charophyta	Zygnemo-phyceae
ClospCPR5.2	GJP75531.1	*Closterium*	Charophyta	Zygnemo-phyceae
KlenitCPR5	GAQ84352.1	*Klebsormidium nitens*	Charophyta	Klebsormidio-phyceae
MesenCPR5	jgi|Mesen1|2959|ME000176S02004	*Mesotaenium endlicherianum SAG 12.97*	Charophyta	Zygnemo-phyceae
MeskraCPR5.1	jgi|Meskra657_3|1148962|CE1148961_11182	*Mesotaenium kramstae Lemmermann NIES-657 v3.0*	Charophyta	Zygnemo-phyceae
MeskraCPR5.2	jgi|Meskra657_3|1148923|CE1148922_14999	*Mesotaenium kramstae Lemmermann NIES-657 v3.0*	Charophyta	Zygnemo-phyceae
SpimuCPR5.1	jgi|Spimu1|7829|SM000018S03736	*Spirogloea muscicola CCAC 0214*	Charophyta	Spiroglo-eophycidae
SpimuCPR5.2	jgi|Spimu1|5703|SM000152S01566	*Spirogloea muscicola CCAC 0215*	Charophyta	Spiroglo-eophycidae
SpimuCPR5.3	jgi|Spimu1|9349|SM000020S05962	*Spirogloea muscicola CCAC 0216*	Charophyta	Spiroglo-eophycidae
BpraCPR5	BPRRCC1105_03G01860	*Bathycoccus prasinos*	Chlorophyta	Mamiello-phyceae
ChlodesCPR5.1	KAH7624053.1	*Chlorella desiccata (nom. nud.)*	Chlorophyta	Trebouxio-phyceae
ChlodesCPR5.2	KAG7670930.1	*Chlorella desiccata (nom. nud.)*	Chlorophyta	Trebouxio-phyceae
ChlosoroCPR5	PRW44950.1	*Chlorella sorokiniana*	Chlorophyta	Trebouxio-phyceae
ChlospCPR5	CNC64A_008G01100	*Chlorella sp NC64A*	Chlorophyta	Trebouxio-phyceae
ChlovarCPR5	XP_005848448.1	*Chlorella variabilis*	Chlorophyta	Trebouxio-phyceae
ChlovulCPR5	KAI3426217.1	*Chlorella vulgaris*	Chlorophyta	Trebouxio-phyceae
ChlpriCPR5	QDZ25445.1	*Chloropicon primus*	Chlorophyta	Chloropico-phyceae
CocsubCPR5	CV00G07110	*Coccomyxa sub-ellipsoidea C-169*	Chlorophyta	Trebouxio-phyceae
MicrocomCPR5	XP_002502434.1	*Micromonas commoda*	Chlorophyta	Mamiello-phyceae
MicropuCPR5	EuGene.0500010166|58433	*Micromonas pusilla strain CCMP1545*	Chlorophyta	Mamiello-phyceae
MicrospCPR5	M.spRCC299 v3.0|58433	*Micromonas sp or commoda RCC299 v3.0*	Chlorophyta	Mamiello-phyceae
OtCPR5	OT_02G03660	*Ostreococcus tauri*	Chlorophyta	Mamiello-phyceae
PispCPR5.1	KAI8111799.1	*Picochlorum*	Chlorophyta	Trebouxio-

		sp. BPE23		phyceae
PispCPR5.2	KAI8109780.1	*Picochlorum sp. BPE23*	Chlorophyta	Trebouxio-phyceae
MapolyCPR5.1	Mapoly0107s0002.1.p	*Marchantia polymorpha_320_v3.1*	Seedless non-tracheophyte	Marchantiopsida
MapolyCPR5.2	Mapoly0483s0001.1.p	*Marchantia polymorpha_320_v3.1*	Seedless non-tracheophyte	Marchantiopsida
MapolyCPR5.3	Mapoly0002s0001.1.p	*Marchantia polymorpha_320_v3.1*	Seedless non-tracheophyte	Marchantiopsida
PpCPR5.1	Pp3c21_530V3.1.p	*Physcomitrium patens_318_v3.3*	Seedless non-tracheophyte	Bryopsida
PpCPR5.2	Pp3c22_5670V3.1.p	*Physcomitrium patens_318_v3.3*	Seedless non-tracheophyte	Bryophyta
SphfalxCPR5	Sphfalx02G141400.1.p	*Sphagnum fallax v1.1*	Seedless non-tracheophyte	Bryophyta
DicomCPR5	Dicom.14G001200.1.p	*Diphasiastrum complanatum v3.1*	Seedless tracheophyte	Lycopodiopsida
CericCPR5	Ceric.38G046900.1.p	*Ceratopteris richardii v2.1*	Seedless tracheophyte	Polypodiopsida
AtriCPR5	ATR_00156G00170	*Amborella trichopoda*	Spermatophyta	Basal angiosperm
AtCPR5	AT5G64930	*Arabidopsis thaliana*	Spermatophyta	Dicot
BradiCPR5.1	Bradi3g57717.1.p	*Brachypodium distachyon v3.1*	Spermatophyta	Monocot
BradiCPR5.2	Bradi2g58840.1.p	*Brachypodium distachyon v3.1*	Spermatophyta	Monocot
CocitCPR5	Cocit.H3845.1.p	*Corymbia citriodora v2.1*	Spermatophyta	Dicot
GlymaCPR5	Glyma.06G145800.1.p	*Glycine max Wm82.a4.v1*	Spermatophyta	Dicot
GohirCPR5.1	Gohir.D03G045400.2.p	*Gossypium hirsutum v3.1*	Spermatophyta	Dicot
GohirCPR5.2	Gohir.A02G134000.1.p	*Gossypium hirsutum v3.1*	Spermatophyta	Dicot
HorvuCPR5.1	HORVU.MOREX.r3.6HG0618780.1	*Hordeum vulgare Morex V3*	Spermatophyta	Monocot
HorvuCPR5.2	HORVU.MOREX.r3.3HG0309890.1	*Hordeum vulgare Morex V3*	Spermatophyta	Monocot
ManesCPR5.1	Manes.13G077600.1.p	*Manihot esculenta v8.1*	Spermatophyta	Dicot
ManesCPR5.2	Manes.12G141400.1.p	*Manihot esculenta v8.1*	Spermatophyta	Dicot
NtCPR5.1	mRNA_71958	*Nicotiana tabacum K326*	Spermatophyta	Dicot
NtCPR5.2	mRNA_118909	*Nicotiana tabacum K326*	Spermatophyta	Dicot
OsCPR5.1	LOC_Os02g53070.1	*Oryza sativa_323_v7.0*	Spermatophyta	Monocot
OsCPR5.2	LOC_Os01g68970.1	*Oryza sativa_323_v7.0*	Spermatophyta	Monocot
PahalCPR5.2	Pahal.5G042600.1.p	*Panicum hallii v3.1*	Spermatophyta	Monocot
PahalCPR5.1	Pahal.1G413600.1.p	*Panicum hallii v3.2*	Spermatophyta	Monocot
PavirCPR5.1-1	Pavir.1KG111437.1.p	*Panicum virgatum v5.1*	Spermatophyta	Monocot
PavirCPR5.1-2	Pavir.1NG487400.1.p	*Panicum virgatum v5.1*	Spermatophyta	Monocot

PavirCPR5.2-1	Pavir.5NG012660.1.p	*Panicum virgatum v5.1*	Spermatophyta	Monocot
PavirCPR5.2-2	Pavir.5KG720000.1.p	*Panicum virgatum v5.1*	Spermatophyta	Monocot
PtrifCPR5	Ptrif.0007s2410.1.p	*Poncirus trifoliata v1.3.1*	Spermatophyta	Dicot
PotriCPR5.1	Potri.005G083600.1.p	*Populus trichocarpa v4.1*	Spermatophyta	Dicot
PotriCPR5.2	Potri.007G082100.1.p	*Populus trichocarpa v4.1*	Spermatophyta	Dicot
SolycoCPR5	Solyc04g054170.4.1	*Solanum lycopersicum ITAG4.0*	Spermatophyta	Dicot
StrasiaCPR5.1	GER47577.1	*Striga_asiatica 008636005.1_SGA_v2.0*	Spermatophyta	Dicot
StrasiaCPR5.2	GER47578.1	*Striga_asiatica_ 008636005.1_SGA_v2.0*	Spermatophyta	Dicot
ThuplCPR5	Thupl.29379795s0007.1.p	*Thuja plicata v3.1*	Spermatophyta	Gymnosperm
VviCPR5	VIT_207s0031g01470.1	*Vitis vinifera v2.1*	Spermatophyta	Dicot
ZmayCPR5.1	Zm00001d052145_P001	*Zea mays RefGen_V4*	Spermatophyta	Monocot
ZmayCPR5.2	Zm00001d012040_P001	*Zea mays RefGen_V4*	Spermatophyta	Monocot
ZosmaCPR5	Zosma03g20130.1	*Zostera marina v3.1*	Spermatophyta	Monocot

table S8. Primers used in this study

Primer	Sequence (5´-3´)	Description
NUP98a_Fw	TACAAAAAAGCAGGCTTCATGTTTGGCTCATCTAATCCTTTTGG	**For localization**
NUP98a_Rv	CAAGAAAGCTGGGTCAACTCCATCTTCTTCATCTTCGT	
NUP155_Fw	TACAAAAAAGCAGGCTTCAAGATGTCACAAGACGATGAG	
NUP155_Rv	CAAGAAAGCTGGGTCGAAGGAGAATGGACTTAAGAGAGACT	
NUP160_Fw	TACAAAAAAGCAGGCTTCATGGAGGAGAATCGTCGG	
NUP160_Rv	CAAGAAAGCTGGGTCACCGGTTGCAGAGGATACAG	
NUP50a_Fw	TACAAAAAAGCAGGCTTCATGGGTGACTCGGAAAACGT	
NUP50a_Rv	CAAGAAAGCTGGGTCAGTATCTGTAGCTGTTGGAGAGT	
NUP214_Fw	TACAAAAAAGCAGGCTTCAAGATGAGCAGAGTTGAGATTGAAG	
NUP214_Rv	CAAGAAAGCTGGGTCTTTTCTCATCTGTGTGAAGAGTTCC	
Rae1_Fw	TACAAAAAAGCAGGCTTCATGGCAACTTTTGGTGCGC	
Rae1_Rv	CAAGAAAGCTGGGTCTTTTCTGCCGGTTGCTCCAA	
Sec13_Fw	TACAAAAAAGCAGGCTTCAACATGCCAGGTCAGAAGATTGA	
Sec13_Rv	CAAGAAAGCTGGGTCAGGCTCAACAGCAGTAACTTGTTCC	
Elys/HOS1_Fw	TACAAAAAAGCAGGCTTCATGGATACGAGAGAAATCAACGGT	
Elys/HOS1_Rv	CAAGAAAGCTGGGTCTCTTGCTGCGAATCTACGTCT	
NUP93a_Fw	TACAAAAAAGCAGGCTTCATGGCGAACGACCAAGAGAT	
NUP93a_Rv	CAAGAAAGCTGGGTCAAAGCTTCGAGCCACCTTCTCG	
NUP62_Fw	TACAAAAAAGCAGGCTTCATGTCGGGGTTTCCATTTGGT	
NUP62_Rv	CAAGAAAGCTGGGTCAGACATCCAGTGCTTTGG	
NUP136_Fw	TACAAAAAAGCAGGCTTCCTAATGGCGAGCGCGGCAC	
NUP136_Rv	CAAGAAAGCTGGGTCTTTCTTCCTGGTGGATTTCTTTGC	
NUP107_Fw	TACAAAAAAGCAGGCTTCATGGATATGGATATGGACACTTCCC	
NUP107_Rv	CAAGAAAGCTGGGTCAGGTGATGAAAGTTCCTCTTGA	
NUP50b_Fw	TACAAAAAAGCAGGCTTCATGGGGGACTCCGATAATGC	
NUP50b_Rv	CAAGAAAGCTGGGTCCCTAGCATCTTCAGCACTCGGTGAG	
NUP35_Fw	TACAAAAAAGCAGGCTTCAAAATGAGTGCTGCAGCACACAGG	
NUP35_Rv	CAAGAAAGCTGGGTCAACACCGAACATCAAGTCAAAGA	
NUP93b_Fw	TACAAAAAAGCAGGCTTCATGGCGAACGACCAGGAG	
NUP93b_Rv	CAAGAAAGCTGGGTCAAAGCTTCGAGCTATCTTCTCG	
NUP43_Fw	TACAAAAAAGCAGGCTTCATGGAGATGATGCAGGATTCGT	
NUP43_Rv	CAAGAAAGCTGGGTCAGGCCTTGAGAAAACTGCTA	
NUP85_Fw	TACAAAAAAGCAGGCTTCAAAATGCCGGGTATGTCTTCGGA	
NUP85_Rv	CAAGAAAGCTGGGTCACATTCTTCGAGAAAAGCACGT	
NUP58_Fw	TACAAAAAAGCAGGCTTCATGTCGTTTTTTCCCCCAC	
NUP58_Rv	CAAGAAAGCTGGGTCTGTACGGCGTGTAGTTCGAGATTTT	
NUP82_Fw	TACAAAAAAGCAGGCTTCGAGTTCATGGCCACTCAAGGAGAAGC	
NUP82_Rv	CAAGAAAGCTGGGTCTGTCTTACAGCAGACACCGTCACTT	
Gp210_Fw	TACAAAAAAGCAGGCTTCATGGTTCCCGTCTCGTTCTG	
Gp210_Rv	CAAGAAAGCTGGGTCCATAGTGTTTTGAGGATTAAACC	
NUP205_Fw	TACAAAAAAGCAGGCTTCATGGTGTCGCCGAAAGATTT	
NUP205_Rv	CAAGAAAGCTGGGTCTACACACTTTTGGATGGCCA	
CPR5_Fw	TACAAAAAAGCAGGCTTCTTTAAGGCTATGGAAGCCCTCCTCC	
CPR5_Rv	CAAGAAAGCTGGGTCCTCGTCAGCATAGTCAGACCCACCA	
GGBmScarlet3F	AAAGGTCTCAAACAATGGACAGTACCGAAGCT	
GGBmScarlet3R	AAAGGTCTCAAGCCGGATCCCCCGGAGC	
PpNUP98.1_Fw	TGTACAAAAAAGCAGGCTTAATGTTTGGATCCAGCAGCCC	
PpNUP98.1_Rv	TGTACAAGAAAGCTGGGTAATCAAAATCCAGACCATATCCACTG	
2_Fw	AAAAAAGCAGGCTTAATGTCGGGCTTCACAGGATT	
PpNup62_Rv	AAGAAAGCTGGGTAGGCTCCACGCAAACGAGATC	
PpNup58_Fw	AAAAAAGCAGGCTTAATGGCGGGGATGTTCCAAAC	
PpNup58_Rv	AAGAAAGCTGGGTACTTTCGACGTGTGCCAC	

PpNup35.1_Fw	TACAAAAAAGCAGGCTTCATGAGTACCCCAGGCGCG	
PpNup35.1_Rv	CAAGAAAGCTGGGTCCATACCAAATACAAAATCCACAAATT	
PDLP5_SIM_Fw	TTTGGTCTCAGGCTCTATGATCAAGACAAAGACGACG	**For SIM**
PDLP5_SIM_Rv	TTTGGTCTCACTGATTTACACCATTTCTCATCTGCA	
CPR5_SIM_Fw	TTTGGTCTCAGGCTCTATGGAAGCCCTCCTCCTC	
CPR5_SIM_Fw	TTTGGTCTCACTGAAGCATAGTCAGACCCACC	
GGDmScarlet3F	AAAGGTCTCATCAGGTATGGACAGTACCGAAGCT	
GGDmScarlet3R	AAAGGTCTCAGCAGGGATCCCCCGGAGC	
CPR5_Topol_Rv	GGGGACCACTTTGTACAAGAAAGCTGGGTATCAAGCATAGTCAGACCCACC	**For CPR5 topology**
mEGFP_Fw	GGGGACAAGTTTGTACAAAAAAGCAGGCTTCACCATGGTGAGCAAGGGCGAGG	**For microparticle bombardment**
mEGFP_Rv	GGGGACCACTTTGTACAAGAAAGCTGGGTGTTACTTGTACAGCTCGTCCATGCC	
2xmEGFP_Fw	GGGGACAAGTTTGTACAAAAAAGCAGGCTTCACCATGGTTTCTAAGGGTGAGG	
2xmEGFP_Rv	GGGGACCACTTTGTACAAGAAAGCTGGGTGTTACTTGTACAGCTCGTCCATGCC	
NUP62_F	GCTTTTTCTATTGAGGTTCAAACTTGTAAGC	**For transgenic line expressing NUP62-GFP**
NUP62_R	CCGGTCAAGAGAAATATAATAATCTCTG	
NUP62_U1	AGACATCCAGTGCTTTGGAGCC	
NUP62_D1	TGATAAGAATTACAAAAACCACATAATCTC	
NUP62GFP_HiFiF	AAGCACTGGATGTCTGGTGGAGGCGGTTCAGGCGGAGGTGG	
NUP62GFP_HiFiR	TTGTAATTCTTATCACTTGTACAGCTCGTCCATGCCGTG	